



# Computational Time Reduction in Meso-Scale Masonry Structure Analysis by Nonlinear Topology Optimization Methods

Nima Khorami<sup>1</sup> · Ali Nikkhoo<sup>2</sup> · Ali Sadollah<sup>1</sup> · Ali Permanoon<sup>3</sup> · Farzad Hejazi<sup>4</sup>

Received: 30 April 2024 / Revised: 29 December 2024 / Accepted: 24 February 2025  
© The Author(s) 2025

## Abstract

This research presents a novel algorithm designed to reduce computational time in the meso-scale analysis of masonry buildings. The algorithm employs nonlinear topology optimization in conjunction with the Drucker-Prager yield criterion to identify critical zones within a structure. These critical zones are modeled at the meso-scale, while less critical regions are represented at the macro-scale. To evaluate the efficacy and accuracy of the proposed method, three masonry wall samples were analyzed, comparing computational time and accuracy across three modeling strategies: full meso-scale, full macro-scale, and optimized meso-macro scale. The results indicate that while macro-scale models provided faster analyses, they exhibited lower accuracy compared to meso-scale models and demonstrated greater initial stiffness and maximum force due to their elastic-perfectly plastic behavior. In contrast, the optimized meso-scale models reduced the computational time by 32.5%, 46%, and 30% compared to full meso-scale models, while maintaining high accuracy in replicating crack patterns and force–displacement responses observed in experimental data. These findings suggest that the developed algorithm offers an efficient and accurate computational approach for analyzing the complex behavior of masonry buildings under various loading conditions.

**Keywords** Meso-scale · Masonry buildings · Topology optimization · Computational time · Semi-brittle materials

## Abbreviations

CAEI Combined accuracy-efficiency index  
CPU Central processing unit  
CZM Cohesive zone model

DEM Discrete element method  
Dof Degrees of freedom  
DP Drucker-prager (Yield surface)  
DW Door wall  
FEM Finite element method  
FM Full meso-scale model  
MC Macro-scale model  
MFT Mesh fragmentation technique  
MLAI Maximum load accuracy index  
NCT Normalized CPU time  
OM Optimized meso-scale model  
SW Shear wall  
TO Topology optimization  
WW Window wall  
XFEM Extended finite element method  
SIMP Solid isotropic material with penalization

✉ Farzad Hejazi  
Farzad.Hejazi@uwe.ac.uk  
  
Nima Khorami  
nimakhorami@stu.usc.ac.ir  
  
Ali Nikkhoo  
nikkhoo@usc.ac.ir  
  
Ali Sadollah  
sadollah@usc.ac.ir  
  
Ali Permanoon  
permanoon.ali@gmail.com

- <sup>1</sup> Department of Civil Engineering, University of Science and Culture, Tehran, Iran
- <sup>2</sup> Department of Mechanical Engineering, University of Science and Culture, Tehran, Iran
- <sup>3</sup> Department of Civil Engineering, Razi University, Kermanshah, Iran
- <sup>4</sup> Department of Civil Engineering, University of The West of England, Bristol, UK

## List of Symbols

$C_0$  Prescribed energy  
 $J_1(\sigma)$  First deviatoric invariants of the stress tensor  
 $J_2(\sigma)$  Second deviatoric invariants of the stress tensor  
 $J_1(\varepsilon)$  First invariant of the strain tensor

$J_2(\varepsilon_d)$	Second invariant of the deviatoric strain tensor
$\alpha, H$	Constants of the DP yield surface
$\phi$	Friction Angle
$C$	Cohesion
$f'_m$	Compressive strength
$f_t$	Tensile strength
$E$	Elastic modulus
$E_m$	Elastic modulus of masonry
$\psi$	Dilatancy angle
$J_U(\rho)$	Objective function
$u(\rho)$	Displacement variable
$\rho$	Density variable
$V$	Volume of the finite element model
$V_{\max}$	Maximum allowed volume
$V_0$	Initial volume
$V^*$	Material volume that needs to be removed
$K$	Stiffness value
$\rho_e$	Density variable for each element
$\rho_{\min}$	Minimum allowed density
$\chi(\rho, u(\rho))$	Adjoint variables
$f_0$	Given load vector
$T(\rho, u(\rho))$	Internal force vector
$\varepsilon_d$	Deviatoric strain tensor
$\phi_1, \phi_2$	Functions representing the hardening behavior of the material
$\sigma$	Stress tensor
$\sigma^L$	Linear elastic limit of the stress tensor
$\sigma^N$	Nonlinear elastic limit of the stress tensor
$\varepsilon$	Strain tensor
$\varepsilon^L$	Linear elastic limit of the strain tensor
$\varepsilon^N$	Nonlinear elastic limit of the strain tensor
$\varphi$	Strain energy density
$\varphi^L$	Linear elastic strain energy density
$\chi$	Reaction load factor
$\bar{\sigma}$	Shear strengths of the contact element
$\bar{\tau}$	Tensile strengths of the contact element
$\delta_n$	Separation values of the contact element in the normal direction
$\delta_t$	Separation values of the contact element in the shear direction
$\delta_n^0$	Normal values of the initial permanent separation
$\delta_t^0$	Shear values of the initial permanent separation
$\delta_n^1$	Normal values of the displacement at the point of fracture
$\delta_t^1$	Shear values of the displacement at the point of fracture
$G_I$	Energy absorbed in the normal direction
$G_{II}$	Energy absorbed in the shear direction
$G_{IC}$	Critical energy release rates in tension

$G_{IIC}$	Critical energy release rates in shear
$D$	Damage index
$U_c$	Structural strain energy
$\eta$	Optimization coefficient
$W$	Weighting coefficient

## 1 Introduction

Structural optimization is generally categorized into three primary categories: size, shape, and topology optimization (TO). The main difference between these categories is the definition of design variables [1]. TO is a key area of structural optimization aimed at determining the optimal material arrangement for a structure within specified constraints [2]. Since the 1980s, rapid advancements in computer technology have significantly enhanced TO methods based on finite element analysis, thereby introducing innovative approaches for identifying optimal structural configurations [3].

Various TO methods have been developed, including Solid Isotropic Material with Penalization (SIMP) [4], level set methods [5], and Evolutionary Structural Optimization (ESO) [6, 7]. The ESO method and its enhanced version, Bidirectional Evolutionary Structural Optimization (BESO), are popular for their simplicity and commercial software availability [8]. ESO removes excess material to achieve an optimal configuration, while BESO allows for the simultaneous removal of inefficient materials and the addition of efficient ones [9]. The BESO enhances the solution process compared to the conventional ESO and is widely used in architecture, aerospace, medicine, and biomechanics [10].

Using classical TO along with suitable design objectives and constraints yields more accurate and efficient solutions, promotes material conservation, and reduces the overall structural weight [11, 12]. TO is crucial for determining the optimal fiber arrangement in composite structures, particularly in materials such as Carbon Fiber-Reinforced Plastics (CFRP) and laminate composites [13]. For masonry structures, assuming structural homogeneity, TO can identify the most effective placement and arrangement of reinforcing fibers [14], and in concrete structures, helps pinpoint the force transmission zones and improve the computational efficiency [15].

Masonry structures, which constitute most historical buildings and remain widely used across various countries because of their numerous advantages, require a thorough investigation of their behavior under stability-threatening conditions. [16, 17]. In contrast to steel and concrete structures, whose behavior can be evaluated using

established guidelines and analytical techniques, the mechanical response of masonry structures is complex, diverse, and nonlinear [18, 19]. Historically, the investigation of masonry structures has relied on costly and time-consuming experiments. However, numerical techniques have emerged as practical alternatives for accurately characterizing their behavior.

Common numerical methods include the Finite Element Method (FEM) [20–22], Extended Finite Element Method (XFEM) [23], fracture mechanics-based methods [24] and Discrete Element Methods (DEM) [25]. Among these, the FEM is particularly effective for analyzing masonry structures under various boundary conditions [21, 22]. The analysis of masonry structures is typically categorized into macro-scale, micro-scale, and meso-scale modeling approaches [18, 26]. Macro-scale modeling assumes structural homogeneity and focuses on the overall behavior, making it cost-effective for large-scale structures, but lacking detailed precision [27].

In micro-scale analysis, each component of a masonry structure is modeled individually to accurately capture the detailed behavior of the entire structure [28, 29]. Micro-scale analysis, while precise, demands significant computational resources owing to the detailed modeling of each component. Consequently, it is often impractical for real-scale masonry structures because of its high computational cost and extended processing time [30]. Meso-scale modeling, a simplified version of micro-scale analysis, is widely used in numerical research [31, 32]. However, it requires significantly more computational time than macro-scale models [27].

Akhaveissy [33] employed a meso-scale numerical model to simulate the dynamic behavior of unreinforced masonry walls under blast loading conditions. Lourenco [34] developed advanced models for the mechanical analysis of masonry structures, employing micro-scale, macro-scale, and multi-scale techniques to simulate various levels of masonry behavior, from component-level analyses to entire monumental buildings. Maccarini [35] used macro-scale finite element models to investigate the out-of-plane behavior of stone masonry structures, identifying the key material and geometric parameters that affect their performance. Gregori [36] proposed a micro-modeling approach to evaluate the effects of defects such as ineffective vertical mortar joints and variability in joint thickness.

The adoption of multi-scale models has become increasingly prominent since the late twentieth century, reflecting the need to balance computational cost and precision. These models have proven particularly beneficial for heterogeneous structures such as masonry. Addressi et al. [37, 38] introduced a multi-scale approach for analyzing masonry structures with curved elements and

periodic textures. They also utilized multi-scale models to examine the behavior of masonry structures under out-of-plane instability [39]. Petracca [40] developed a multi-scale computational homogenization method focusing on periodic brick-masonry walls. Mercatoris and colleagues presented a multi-scale framework for analyzing the failure of periodic quasi-brittle thin planar shells [41]. Integrating multi-scale models with TO enhances computational efficiency, as demonstrated by Sivapuram's [42] novel multi-scale optimization strategy, which optimizes the design at both macro- and micro-scales.

This paper presents an algorithm developed to reduce the computational cost associated with the analysis of meso-scale masonry buildings. The algorithm is based on nonlinear TO and employs the Drucker-Prager (DP) yield surface. During the TO analysis, strain energy is maximized through a nested optimization approach while adhering to specified volume constraints. Subsequently, three masonry wall samples, previously examined by researchers through laboratory experiments, are analyzed on a macro-scale using the nonlinear TO algorithm. Effective regions for force transmission are identified as critical regions. In a two-scale model, these critical regions are represented at the meso-scale, while the remaining regions are modeled at the macro-scale. The results of the analysis, along with the associated computational costs, are compared to those of the initial models that are entirely modeled at the meso-scale, and these findings are further contrasted with experimental results.

## 2 Development of Computational Time Reduction in Meso-Scale Masonry Structure Analysis

In the macro-scale modeling of masonry structures, the mechanical behavior of the entire assembly is represented as a homogenized composite material, without explicitly modeling the individual masonry units and mortar layers. While this approach can approximate the overall crack distribution through methods such as the smeared crack approach, it fails to capture detailed interactions, including localized sliding and deformation between masonry units. Although it offers a computationally efficient solution, this method sacrifices detail, resulting in reduced accuracy when compared to micro and meso-scale models. Conversely, micro-scale models provide a highly detailed representation by modeling each masonry unit, mortar layer, and their interactions individually. This level of detail facilitates a comprehensive understanding of the mechanical behavior at the material level; however, it necessitates substantial computational resources due to the high number of degrees of freedom involved, rendering it

impractical for large-scale applications. Meso-scale models, on the other hand, strike a balance between detail and computational efficiency by simplifying the micro-scale approach. In meso-scale modeling, the masonry units are modeled individually, while the mortar is not explicitly represented; instead, its effects are simulated using contact elements between the units. This methodology allows for the observation of key local behaviors, such as sliding and deformation between masonry units. Although meso-scale modeling incurs a higher computational cost than macro-scale methods, it achieves significantly greater accuracy in representing failure mechanisms and local interactions, thereby providing a more realistic prediction of the structural response under various loading conditions [43, 44]. Figure 1 illustrates the representation of masonry modeling at the macro, meso, and micro-scales.

To clarify the foundational concept of this research, as illustrated in Fig. 2, the primary objective is to reduce the computational time required for analyzing a masonry wall at the meso-scale under specified boundary conditions. The initial analysis is conducted using the TO approach at the macro-scale, which is based on a nonlinear elastic model incorporating the Drucker-Prager yield criterion. This criterion allows for more accurate identification of critical regions by tracing the paths of internal forces, including tensile and compressive forces. The optimization framework maximizes strain energy within specified volume constraints through a nested iterative process, identifying regions with the highest strain energy as critical load paths. These critical regions, highlighted in green in Fig. 2b, are essential for effective force transmission.

Unlike classical TO methods that typically utilize yield surfaces such as the von Mises criterion—which assumes uniform material behavior in both tension and compression—this approach tackles the challenges posed by materials like masonry, which exhibit distinct behaviors under tension and compression. By incorporating the Drucker-Prager criterion, the developed algorithm more

accurately identifies the load transfer path by pinpointing regions with high plastic stress and strain as critical.

Following this, the initial model is reanalyzed using a two-scale approach, informed by the results of the TO analysis. Notably, only the green regions are modeled at the meso-scale, while the remaining areas are represented at the macro-scale, acknowledging that not all components of a structure contribute equally to force transfer. This methodology is designed to reduce the degrees of freedom in the structural analysis process. Following this, the initial model is reanalyzed at a two-scale approach, informed by the results of the TO analysis. Notably, only the green regions are modeled at the meso-scale, while the remaining areas are represented at the macro-scale, acknowledging that not all components of a structure contribute equally to force transfer. This methodology is designed to reduce the degrees of freedom in the structural analysis process [45, 46].

## 2.1 Flowchart of Meso-scale Model Using Topology Optimization

The following steps are pursued to reduce the computational times of analysis masonry buildings at the meso-scale given as follows:

1. Modeling the numerical model at the macro-scale, incorporating the assignment of material properties and the determination of the value of prescribed energy ( $C_0$ ). It is important to note that if the calculation of  $C_0$  from experimental results is not feasible, an initial nonlinear analysis is conducted at the macro-scale, from which  $C_0$  is subsequently derived based on the outcomes of the numerical analysis.
2. The nonlinear analysis of the numerical model at the macro-scale is conducted, employing the TO algorithm to identify regions that are effective in force transmission, referred to as critical regions.

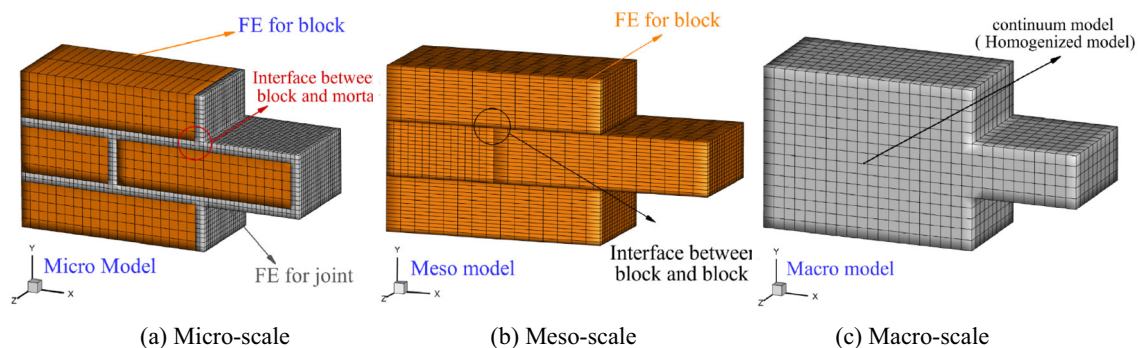
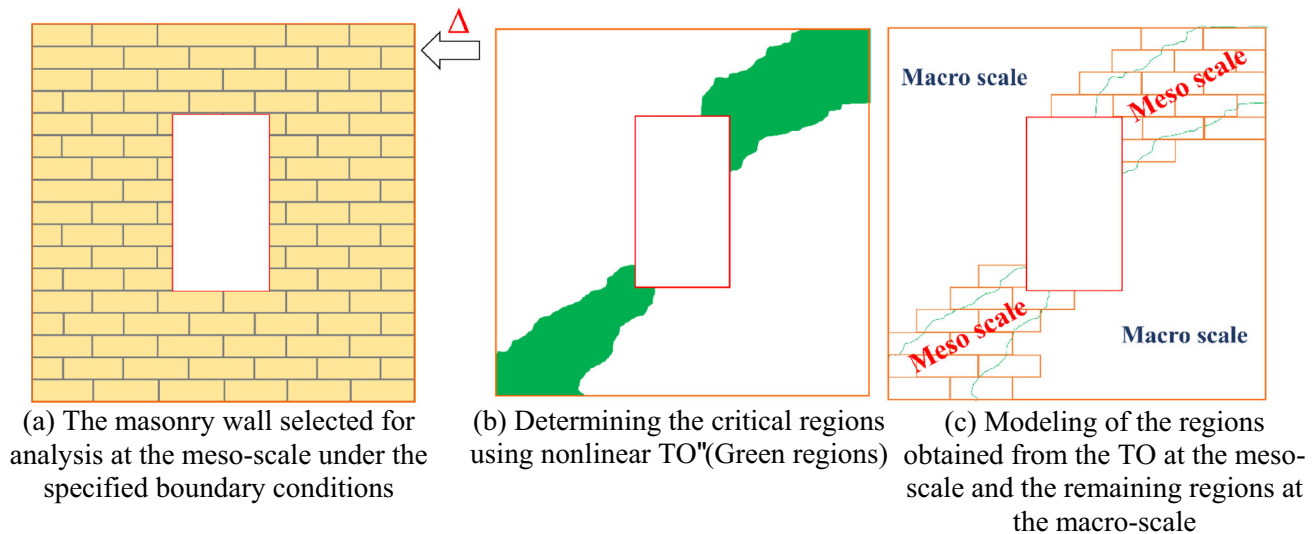


Fig. 1 A representation of masonry numerical models in various scales



**Fig. 2** A demonstration of the developed method in this research study for reducing computational time in the analysis of masonry buildings at the meso-scale

- Two-scale numerical modeling based on the analysis results from the previous stage. In this phase, the critical regions identified by TO are modeled at the meso-scale, while the remaining regions are modeled at the macro-scale.
- Assigning material properties specific to each region and conducting a nonlinear analysis of the intended model.

The optimization algorithm operates based on the values of strain energy and volume constraints. The strain energy value is significantly affected by the material's behavior. Assuming linear elastic behavior for masonry materials yields inaccurate results, as these materials demonstrate different responses to tension and compression due to their brittle nature. Therefore, to calculate the strain energy for each element, the DP yield surface is utilized to account for the brittle behavior of masonry materials.

The procedure illustrated in the flowchart in Fig. 3 has been detailed. In this investigation, the FEM provided by ANSYS software is utilized. The optimization segment, implemented in Fortran, is integrated into ANSYS as a macro phase.

### 3 Governing Equations

In this section, we examine the characteristics of semi-brittle materials at the macro-scale and delineate the nonlinear TO approach employed to identify critical regions. As outlined in Sect. 2, the nonlinear TO formulation was developed to maximize strain energy. The DP yield surface was selected for optimization at the macro-scale. In this

study, a nested optimization framework was utilized to maximize strain energy while adhering to specified volume constraints. The TO formulation is based on nonlinear behavior and seeks to optimize strain energy through the application of the DP yield surface. To manage computational complexity and reduce the volume of calculations while maintaining an acceptable level of accuracy, we adopted the DP criterion. This selection effectively balances accuracy and computational efficiency, aligning to achieve an optimized design within feasible computational limits.

#### 3.1 Behavior of Semi-brittle Materials at the Drucker-Prager Yield Surface

Given that masonry structures exhibit semi-brittle behavior, predicting their response requires the DP yield surface. This surface was formulated in 1952 [47] according to Eq. (1) and is used to predict the behavior of these materials as follows:

$$F(\sigma) = \alpha J_1(\sigma) + \sqrt{J_2(\sigma)} - H \quad (1)$$

where  $J_1(\sigma)$  and  $J_2(\sigma)$  are the first and second deviatoric invariants of the stress tensor, respectively, and  $\alpha$  and  $H$  are constants of the DP yield surface, which vary based on the material's strength properties. These can be expressed by the internal friction angle  $\phi$  and cohesion  $C$ , as shown in Eq. (2) [48, 49] as given by the following equation:

$$\alpha = \frac{2 \sin(\phi)}{\sqrt{3}(3 - \sin(\phi))}, H = \frac{6C \cos(\phi)}{\sqrt{3}(3 - \sin(\phi))} \quad (2)$$

Some materials, such as concrete and masonry, can be characterized by particular compressive strength ( $f'_m$ ) and

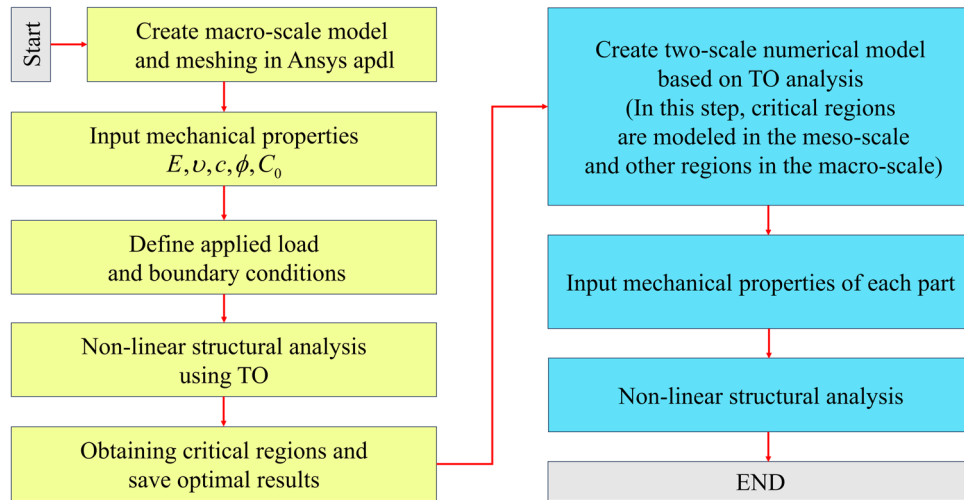


Fig. 3 Flowchart of Meso-scale modeling using the TO approach

tensile strength ( $f_t$ ). In this contexts, one can substitute two specific principal stress states, ( $\sigma_1 = \sigma_2 = 0$ ,  $\sigma_3 = -f'_m$ ) and ( $\sigma_1 = f_t$ ,  $\sigma_2 = \sigma_3 = 0$ ) into the yield condition of Eq. (1) [49] as follows:

$$\begin{cases} -\alpha f'_m + \frac{1}{\sqrt{3}} f'_m - H = 0 \\ \alpha f_t + \frac{1}{\sqrt{3}} f_t - H = 0 \end{cases} \quad (3)$$

Solving Eq. (3) for  $\alpha$  and  $H$  easily leads to the following equations:

$$\alpha = \frac{f'_m - f_t}{\sqrt{3}(f'_m + f)}, \quad H = \frac{2f'_m f_t}{\sqrt{3}(f'_m + f)} \quad (4)$$

Therefore, by equating Eq. (2) and Eq. (4), the  $\phi$  and  $C$  can be expressed based on  $f'_m$  and  $f_t$  provided as in Eq. (5):

$$\phi = \text{Sin}^{-1} \left( \frac{3(f'_m - f_t)}{3f'_m + f_t} \right), \quad C = \frac{f'_m f_t (3 - \sin(\phi))}{3 \cos(\phi) (f'_m + f_t)} \quad (5)$$

In Eq. (5), the values of  $f'_m$  and  $f_t$  is obtained from experimental results. Moreover, if tensile strength is not available, Eq. (6) can be used [50].

$$0.03f'_m < f_t < 0.09f'_m \quad (6)$$

If the value of the elastic modulus of masonry is not available, one can use the proposed FEMA formula (see Eq. (7)) [51]:

$$E_m = 550f'_m \quad (7)$$

Other relationships between compression-tensile strength and the values of cohesion and the friction angle have also been proposed in the literature, as presented in Eq. (8) [52] and Eq. (9) [53] as shown in the following equations:

$$C = \frac{f'_m \cdot f_t}{2\sqrt{f'_m \cdot (f'_m - 2f_t)}}, \quad \phi = \text{sin}^{-1} \left( \frac{f'_m - 4f_t}{f'_m - 2f_t} \right) \quad (8)$$

$$C = 0.5\sqrt{f'_m \cdot f_t}, \quad \phi = \text{Sin}^{-1} \left( \frac{f'_m - f_t}{f'_m + f_t} \right) \quad (9)$$

The dilatancy angle ( $\psi$ ) is another parameter of the DP plasticity model, typically derived from experimental results. However, if experimental determination is not feasible, the relationship provided in Eq. (10) associated with DP plasticity models can be utilized. This is particularly relevant in the field of soil mechanics and other applications involving frictional materials, such as concrete or masonry.

$$\frac{f_t}{\sqrt{2}f'_m} < \tan \psi < \frac{1}{\sqrt{2}} \quad (10)$$

### 3.2 Formulation of Nonlinear Topology Optimization

The formulation of TO in this section is based on nonlinear behavior, aiming to maximize the strain energy of the structure using the DP yield surface. This approach is based on the formulation represented by Eq. (11):

$$\max_{\rho} J_U(\rho) = U(\rho, u(\rho)) \text{ s.t. } \begin{cases} \sum_{e=1}^n \rho_e v_e \leq V_{\max} \\ 0 < \rho_{\min} \leq \rho_e \leq 1 \end{cases} \quad (11)$$

$$\text{with } \begin{cases} T(\rho, u(\rho)) = \chi(\rho, u(\rho)) f_0 \\ f_0^T u(\rho) = 2C_0 \end{cases}$$

The objective function to be maximized is denoted as  $J_U(\rho)$ , which is a function of the density variable ( $\rho$ ) and the displacement variable ( $u(\rho)$ ). The constraint set is

defined by two constraints. The first constraint limits the total volume of the structure, which  $\sum_{e=1}^n \rho_e v_e$  represents the total volume of the structure and  $V_{\max}$  is the maximum allowed volume.

The second constraint imposes bounds on the density variable for each element ( $\rho_e$ ), where  $\rho_{\min}$  is the minimum allowed density and 1 is the maximum allowed density [1]. The variables  $u(\rho)$  and  $\chi(\rho, u(\rho))$  are displacement and adjoint variables, respectively, and  $f_0$  is a given load vector and  $C_0$  is prescribed energy. The equation  $T(\rho, u(\rho)) = \chi(\rho, u(\rho))f_0$  represents the equilibrium equation, where  $T(\rho, u(\rho))$  is the internal force vector and  $\chi(\rho, u(\rho))$  is the adjoint variable. The equation  $f_0^T u(\rho) = 2C_0$  represents a constraint on the displacement variable  $u(\rho)$ .

The optimization problem seeks to identify the density variable that maximizes the objective function while adhering to the specified constraints [54]. The nonlinear yield surface within the DP framework in the strain energy space is represented as a function of  $\varphi(J_1(\varepsilon), J_2(\varepsilon_d))$ , as shown in Eq. (12). The primary goal of the optimization problem is to maximize the function  $U(\rho, u(\rho))$  over the specified domain. This is achieved by integrating the  $\phi$  function. The functions  $\phi_1 = (J_1(\varepsilon), J_2(\varepsilon_d))$  and  $\phi_2 = (J_1(\varepsilon), J_2(\varepsilon_d))$  represent the hardening behavior of materials. Further details are provided in [47, 55, 56]. This function exhibits three distinct regions at the yield surface, as illustrated in Fig. 4.

$$\sigma = \frac{\partial \varphi(J_1(\varepsilon), J_2(\varepsilon_d))}{\partial \varepsilon} \tag{12}$$

Region 1: Linear Zone if  $f(\sigma^{rr}) \leq 0$  (i.e.,  $\phi_1 = \phi_2 = 0$ )

$$\sigma = \frac{1}{2} \sigma^{rr} : \varepsilon' \tag{13}$$

Region 2: Nonlinear Zone if  $f(\sigma^{rr}) > 0$  and  $\phi_2 > 0$

$$\varphi = \varphi^L + \int_0^1 \sigma'(\varepsilon'(t)) dt : (\varepsilon - \varepsilon^L) \tag{14}$$

In Eq. (15),  $\varphi^L$  indicates the value of linear elastic strain energy given as follows:

$$\varphi^L = \frac{1}{2} \sigma^L : \varepsilon^L \tag{15}$$

where  $\sigma^L$  and  $\varepsilon^L$  denote the linear elastic limits of stress and strain tensors, respectively.  $\varepsilon^L$  signifies an interpolation, and  $\varepsilon^L$  represents the strain tensor, as outlined follows:

$$\varepsilon' = (1 - t)\varepsilon^L + t\varepsilon \tag{16}$$

The increment in stress remains constant concerning the strain at the DP yield surface:

$$\sigma' = (1 - t)\sigma^L + t\sigma \tag{17}$$

where  $\sigma^L$  is the interpolated value of  $\sigma^L$  in the stress tensor. By substituting Eq. (17) into Eq. (14), the explicit expression for the strain energy density is derived as follows:

$$\varphi = \frac{1}{2} (\sigma^L : \varepsilon + \sigma : \varepsilon - \sigma : \varepsilon^L) \tag{18}$$

As commonly understood,  $\sigma^L$  and  $\varepsilon^L$  in scalar form can be represented as follows:

$$\sigma^L = t^L \sigma^{rr}, \varepsilon^L = t^L \varepsilon \tag{19}$$

By substituting Eq. (19) into Eq. (18), we can express:

$$\varphi = \frac{1}{2} [t^L (\sigma^{rr} - \sigma) + \sigma] : \varepsilon' \tag{20}$$

Region 3: If  $f(\sigma^{rr}) > 0$  and  $\phi_2 < 0$

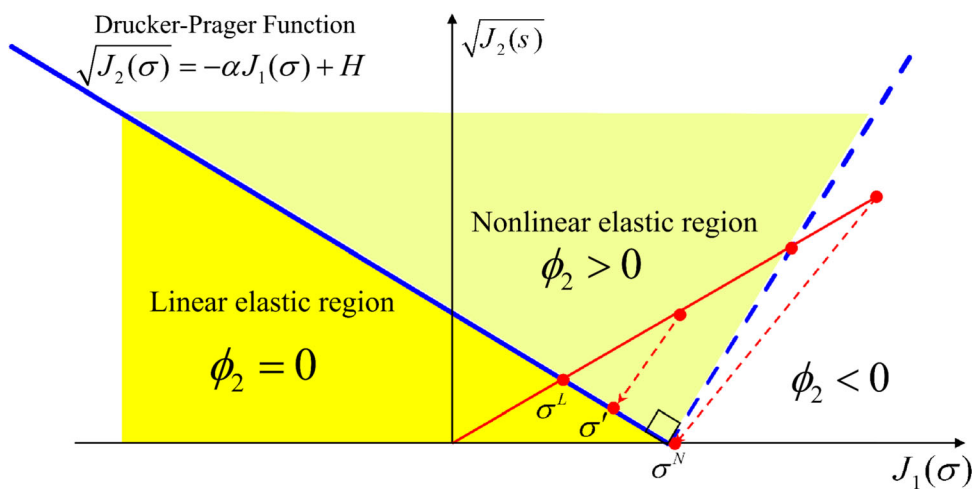


Fig. 4 Visual representation of the stress state according to the DP nonlinear elastic yield criterion

$$\varphi = \frac{1}{2} \sigma^L : \varepsilon^L + \int_{t^L}^{\varepsilon^N} \sigma' : d\varepsilon' + \sigma^N : (\varepsilon - \varepsilon^N) \tag{21}$$

As understood,  $\sigma^N$  and  $\varepsilon^N$  represent the nonlinear elastic limits of stress and strain tensors.

$$\varepsilon' = t\varepsilon, \sigma' = \frac{\sigma^N - \sigma^L}{t^N - t^L} (t - t^L) + \sigma^L \tag{22}$$

By substituting Eq. (22) into Eq. (21), we have:

$$\begin{aligned} \varphi &= \frac{1}{2} \sigma^L \\ &: \varepsilon^L + \int_{t^L}^{\varepsilon^N} \left[ \frac{\sigma^N - \sigma^L}{t^N - t^L} (t - t^L) + \sigma^L \right] : \varepsilon dt + \sigma^N : (\varepsilon - \varepsilon^N) \end{aligned} \tag{23}$$

Through analytical solving and integrating Eq. (23), and substituting the scalar forms of stress and strain, we obtain:

$$\varphi = \frac{1}{2} \sigma^L : \varepsilon^L + \frac{1}{2} (t^N - t^L) (\sigma^N + \sigma^L) : \varepsilon + \sigma^N : (\varepsilon - \varepsilon^N) \tag{24}$$

By substituting  $\sigma^L = t^L \sigma^{tr}$ ,  $\varepsilon^L = t^L \varepsilon^{tr}$  and  $\varepsilon^N = t^N \varepsilon$  into Eq. (24), the strain energy density is succinctly transformed to Eq. (25):

$$\varphi = \frac{1}{2} [(2 - t^L - t^N) \sigma^N + t^L t^N \sigma^{tr}] : \varepsilon' \tag{25}$$

Identifying a solution for Eq. (11), it is equivalent to solving the problem of minimizing with equality, which can be formulated as follows [57, 58]:

$$\begin{cases} \min U(\rho, u(\rho)) \\ s.t. f_0^T = 2C_0 \end{cases} \tag{26}$$

Equation (26) can be solved using a search strategy, such as the Newton–Raphson method with a line search strategy. The set  $A$  is defined as Eq. (27). Therefore, Eq. (26) can be resolved using methods of constraint optimization provided in Eq. (28):

$$A = \{u | f_0^T u = 2C_0\} \tag{27}$$

$$\min_{u \in A} U(\rho, u(\rho)) \tag{28}$$

The objective function can be rewritten as Eq. (29), which means finding the maximum value of the minimum objective function  $J_U(\rho)$  over all feasible solutions  $U$  [59]:

$$\max_{\rho} J_U(\rho) = \max_{\rho} \min_{u \in A} U(\rho, u(\rho)) \tag{29}$$

The sensitivity analysis of this expression is given by Eq. (30) where  $\rho_e$  is a design variable.

$$\frac{dJ_U(\rho)}{d\rho_e} = \frac{\partial U(\rho, u(\rho))}{\partial \rho_e} \tag{30}$$

Introducing an additional adjunct problem in Eq. (30) is unnecessary due to the continuous nature of the relationship. The structure of the strain energy function is as given in Eq. (31) [60]. Therefore, the sensitivity function is derived as Eq. (32):

$$U(\rho, u(\rho)) = \sum_{e=1}^n \int V_e \varphi_e(\rho, u(\rho)) dV \tag{31}$$

$$\frac{dJ_U(\rho)}{d\rho_e} = \sum_{e=1}^n \int V_e \frac{\partial \varphi_e(\rho, u(\rho))}{\partial \rho_e} dV \tag{32}$$

### 3.3 Prescribed Energy

The topological analysis performed in this study employed a nested optimization formula to maximize strain energy while adhering to a volume constraint. The developed method involves iterative optimization cycles to achieve the most optimal design. Central to this process is the prescribed energy value  $C_0$ , which plays a crucial role. Figure 5 visually represents this energy control strategy within the context of systems with two degrees of freedom.

The TO analysis conducted in this study utilized a nested optimization formula to maximize strain energy while adhering to a volume constraint. The developed method involves iterative optimization cycles to achieve the optimal design. Central to this process is the prescribed energy value, which plays a crucial role. Figure 5 visually illustrates this energy control strategy within the context of systems with two degrees of freedom.

The selection of the appropriate  $C_0$  value holds significant importance and can be determined by considering the expected nonlinear behavior as guided by the energy control approach [15, 54, 57].  $C_0$  expressed as the sum of  $C_{01}$  and  $C_{02}$ , representing the area of shaded triangles, which remains constant across all design cycles to attain the optimal design solution. In the context of this illustrative case study, which can be extended to both bi-axial and multi-degrees of freedom scenarios, it is assumed that two reference forces ( $f_{01} < f_{02}$ ) are applied to two distinct degrees of freedom. Moreover, the parameter  $\chi_k > 1$  represents the load factor during the  $k - th$  design cycle. Looking at Figs. 5a and 4b, provide insight into the relationship between reaction force and displacement for each degree of freedom. Figure 5 highlights the energy prescribed during various stages of the process, including the initial optimization iteration (red region in Fig. 5), the first iteration (blue region in Fig. 5), the general  $k - th$  iteration (yellow regions in Fig. 5), and the ultimate optimal design (green regions in Fig. 5). By summing the shaded areas of

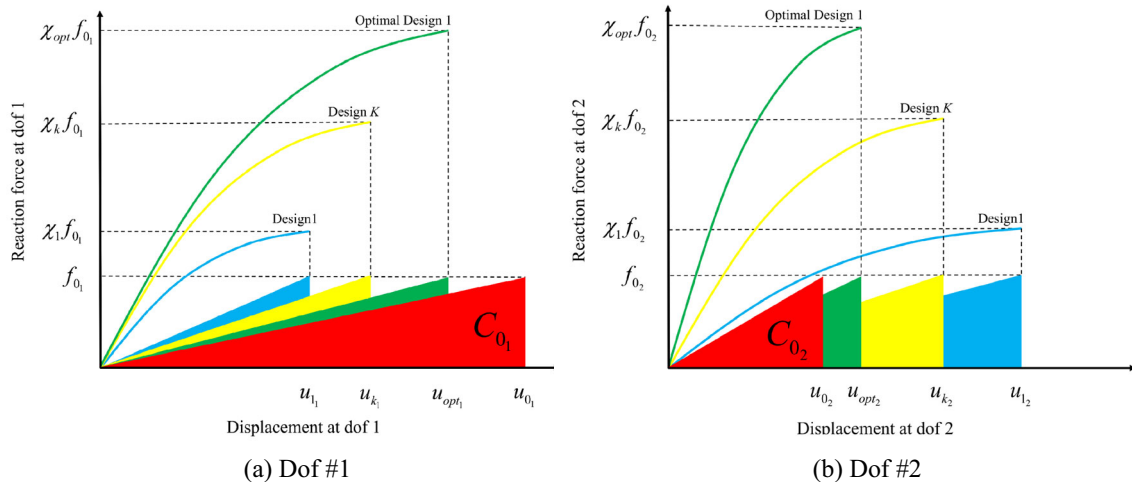


Fig. 5 Visually representation of energy control strategy in the context of systems with 2 degrees of freedom

the same color, a constant value is derived, referred to as the prescribed energy  $C_0$ . This comprehensive approach aims to establish a clear link between energy control and the achievement of optimal design outcomes.

### 3.4 Masonry Structures Modeling

To model the intended masonry walls at the meso-scale, the Mesh Fragmentation Technique (MFT) is utilized. This approach involves the representation of both horizontal and vertical joints, as well as the incorporation of contact elements at the interfaces between blocks, specifically at the meso-scale level (see Fig. 6).

The nonlinear behavior of brick elements was accounted for by employing the Menetrey-Willam [61, 62] yield surface (see Fig. 7). This yield surface considers the material’s behavior under tension and compression.

At the meso-scale, both horizontal and vertical mortar interfaces need to possess the capability for separation and sliding. To accurately model the behavior of mortar, the cohesive crack model was employed between elements. The Cohesive Zone Model (CZM), as formulated by Alfano and Crisfield [63], addresses mechanical

limitations, such as the linear elastic singular stress at crack tips, and ensures a reduction of these constraints during the process of crack propagation. This methodology models crack propagation by the stress-separation law [64, 65]. As illustrated in Fig. 8, the CZM employs exponential models to calculate normal and shear stresses between elements (refer to Eqs. (33) to (36)):

$$\sigma = \begin{cases} \frac{\bar{\sigma}}{\delta_n^0} \delta_n, & \text{if } \delta_n < \delta_n^0 \\ \frac{\delta_n^1 - \delta_n}{\delta_n^1 - \delta_n^0} \bar{\sigma}, & \text{if } \delta_n^0 < \delta_n < \delta_n^1 \\ 0, & \text{if } \delta_n \geq \delta_n^1 \end{cases} \quad (33)$$

$$|\tau| = \begin{cases} \frac{\delta_t}{\delta_t^0} (\bar{\tau} + \tau_f), & \text{if } |\delta_t| < \delta_t^0 \\ \frac{\delta_t^1 - \delta_t}{\delta_t^1 - \delta_t^0} (\bar{\tau} + \tau_f), & \text{if } \delta_t^0 < |\delta_t| < \delta_t^1 \\ \tau_f, & \text{if } |\delta_t| \geq \delta_t^1 \end{cases} \quad (34)$$

$$\tau_f = \begin{cases} -\mu\sigma & \text{if } \sigma < 0 \\ 0 & \text{if } \sigma > 0 \end{cases} \quad (35)$$

$$D = \sqrt{\left(\frac{G_I}{G_{IC}}\right)^2 + \left(\frac{G_{II}}{G_{IIC}}\right)^2} \quad (36)$$

In this context  $\bar{\sigma}$  and  $\bar{\tau}$  represent the shear and tensile strengths of the contact element, respectively. The variables  $\delta_n, \delta_t$  indicate the separation values of the contact element in the normal and shear directions, respectively. Additionally,  $\delta_n^0, \delta_t^0$  denote the normal and shear values of the initial permanent separation, while  $\delta_n^1, \delta_t^1$  represent the normal and shear values of the displacement at the point of fracture. The Level 2 fracture energy criterion integrates various fracture modes [66]. Furthermore,  $G_{IC}, G_{IIC}$  signify

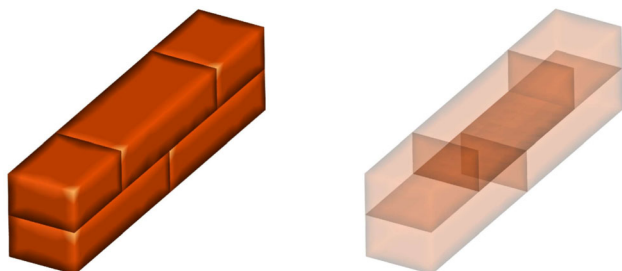


Fig. 6 General view of modeling masonry structures at the meso-scale using the MFT

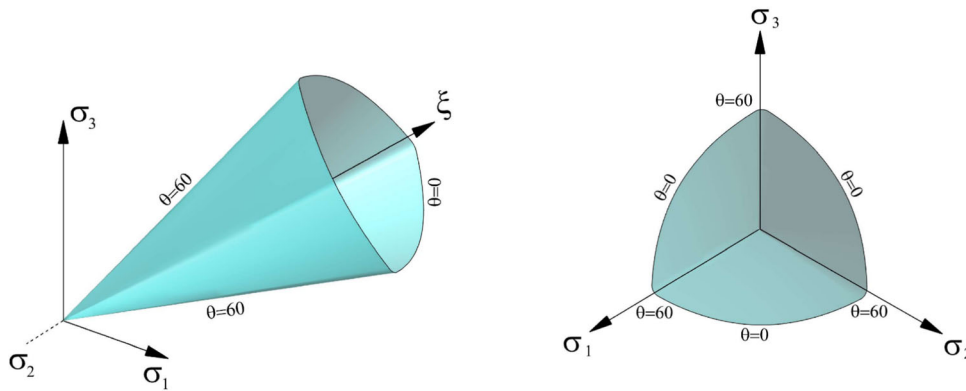


Fig. 7 Three-dimensional Menetrey-Willam yield surface in the principal stress space

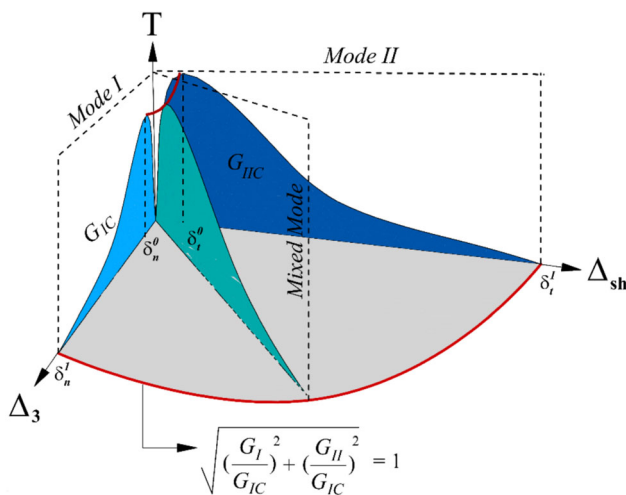


Fig. 8 The utilized CZM model in this research

the critical energy release rates in tension and shear (fracture toughness), respectively, and  $G_I$ ,  $G_{II}$  indicate the energy absorbed in the normal and shear directions. Lastly,  $D$  represents the damage index, which ranges from 0 to 1.

## 4 Numerical Results and Discussions

In this section, three samples of masonry walls previously studied [67–70] at the laboratory scale were modeled in three states: Macro-Scale (MC), Optimized Meso-scale (OM), and Full Meso-scale (FM) to validate the algorithm. The optimization results were compared with the experimental findings.

The numerical models were developed and analyzed using ANSYS APDL software, with the TO process formulated as a nested algorithm coded in Fortran and integrated into ANSYS. To simulate material behavior, the DP failure criterion was implemented.

Nonlinear equations were solved using the modified Newton–Raphson method to handle convergence, with

criteria set at  $u = 0.001$  and  $f = 0.001$ , ensuring both accuracy and stability during the analysis.

The optimization process was performed over 11 steps. In the first step, a vertical load was applied using 5 sub-steps according to the boundary conditions. The remaining 10 steps comprised the TO process, each consisting of 100 sub-steps.

For the FM, OM, and MC models, the analyses were conducted in two steps. In the first step, a vertical load was applied over 5 sub-steps, following the boundary conditions of the problem. The second step involved the main analysis, with the number of sub-steps adjusted based on the model scale. MC models were analyzed with 100 sub-steps, while FM and OM models used 1000 sub-steps.

PLANE182 elements with DP behavior were employed for the MC models and the macro-scale regions of the OM models. For representing bricks, PLANE182 elements with Menetrey-Willam behavior were used in the FM models and the meso-scale regions of the OM models. Additionally, CONTA172 and TARGE169 elements were integrated into both the FM models and the meso-scale regions of the OM models, using the CZM to simulate the interactions between masonry units and connection between the meso-scale and macro-scale parts within the OM models.

To minimize the computational cost of the analyses conducted in this study, 2D models were employed. The proposed methodology is also applicable to 3D multi-layered masonry walls featuring various brick-bond patterns. This adaptability stems from the nearly independent in-plane behavior of masonry walls, regardless of the layer and bond configuration.

### 4.1 Numerical Models

The first and second samples represent two distinct sides of a two-story masonry structure that was experimentally studied by Magenes at Pavia University [67]. The structure features a regular plan with 6.4 m by 4.4 m and a height of

4.6 m, with wall thickness measuring 0.25 m. On one side of the structure, there are two doors on the first floor, each measuring 0.94 m in width and 2.52 m in height. Additionally, there are two windows on the second floor, positioned parallel to the doors below, each also measuring 0.94 m in width and 2.31 m in height.

On the opposite side of this structure, there are three windows on the first floor and three corresponding windows on the second floor, each measuring 0.93 m in width and 1.235 m in height. The floors of both levels have been designed to be rigid, with vertical loads of 248.4 kN and 236.8 kN applied to the first and second floors, respectively. Additionally, a lateral force has been applied cyclically to the floors of this structure (see Fig. 9).

In the modeling process, walls with doors are designated as “DW” (Door-Wall), while walls containing only windows are labeled as “WW” (Window-Wall). For comprehensive details regarding this structure, additional information can be found in the literature [68]. In the third sample, the shear wall proposed by Vermeltfoort and colleagues [69, 70] was subjected to modeling. In the modeling process this wall labeled as “SW” (Shear-Wall) This wall has a width of 0.99 m and a height of 1.0 m. Two rigid steel beams were utilized at the top and bottom of the wall to facilitate experimental control. An average uniform vertical load of 0.3 MPa was applied to the top of the wall. Furthermore, a controlled horizontal displacement was

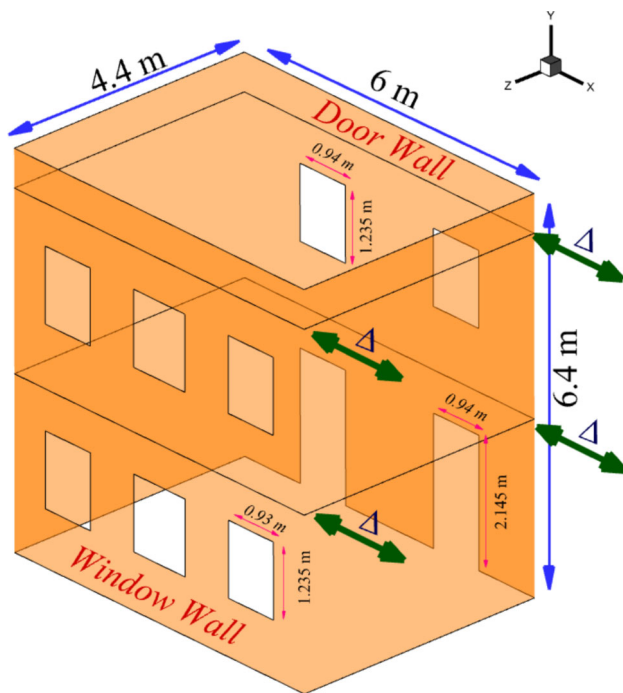


Fig. 9 Structural geometry and applying lateral load of the tested masonry building at the University of Pavia

applied to the top of the wall while the upper portion was held in a fixed vertical position (see Fig. 10).

As stated in the flowchart shown in Fig. 3, the first step in utilizing the developed method involves numerical modeling of the masonry structure at the macro-scale and assigning the material properties and boundary conditions. In this research, the mechanical properties of the models at macro-scale have been determined using Eq. (5) based on the  $f'_m$  parameter obtained from the experimental results. Additionally, the  $E$  and  $f_t$  were determined by using Eqs. (6) and (7). It is worth noting that these same mechanical properties were utilized in the TO analysis. The values of  $C$  and  $\phi$  for the SW, WW, and DW walls in nonlinear analysis at the macro-scale are calculated as provided in Tables 1 and 2. Also, in Tables 1 and 2, the results of Eqs. (5), (8), and (9) using the Mohr–Coulomb equation under vertical load are presented.

In Table 3, the mechanical properties of the numerical models at the meso-scale are presented. For the modeling of masonry units, solid elements with three degrees of freedom were utilized for each node. Additionally, the interface between the bricks and mortar was modeled using contact elements. In continuation, based on the flowchart shown in Fig. 3, the models were analyzed nonlinearly to identify critical regions. All numerical models were analyzed in a two-step process. First, vertical loads were applied, followed by lateral loads according to the experimental samples. Considering the cyclic loading of the “DW” and “WW” models in the laboratory experiment, quasi-static displacement was employed to

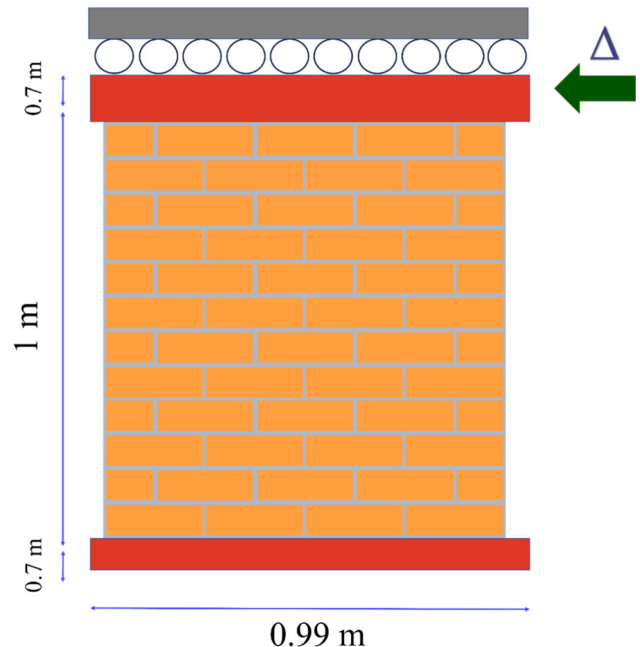


Fig. 10 Geometry and boundary conditions of the shear wall proposed by Vermeltfoort and his colleagues

**Table 1** Mechanical properties of the SW numerical model at the macro-scale using various relationships reported in Sect. 3.1

Masonry Prism	$E_m$ (MPa)	$\nu$	$f_t$ (MPa)	$f'_m$ (MPa)	$C$ (MPa)	$\phi^o$	$\sigma$ (Normal Stress)	$\tau = C + \sigma \tan(\phi)$
Equation (5)	5775	0.15	0.36	10.5	0.8	72.7	0.3	1.76
Equation (8)	5775	0.15	0.36	10.5	1	67.87	0.3	1.73
Equation (9)	5775	0.15	0.36	10.5	0.98	69	0.3	1.76

**Table 2** Mechanical properties of the DW and WW numerical models at the macro-scale using various relations reported in Sect. 3.1

Masonry Prism	$E_m$ (MPa)	$\nu$	$f_t$ (MPa)	$f'_m$ (MPa)	$C$ (MPa)	$\phi^o$	$\sigma$ (Normal Stress)	$\tau = C + \sigma \tan(\phi)$
Equation (5)	3410	0.2	0.18	6.2	0.43	74	0.1	0.78
Equation (8)	3410	0.2	0.18	6.2	0.54	69.7	0.1	0.8
Equation (9)	3410	0.2	0.18	6.2	0.53	70	0.1	0.8

**Table 3** Mechanical properties of numerical models at meso-scale

DW – WW materials	$E$ (GPa)	$\nu$	$C$ (MPa)	$\phi^o$	$G_I$ (N/mm)	$G_{II}$ (N/mm)	$f'_m$	$f_t$	$\psi^o$	$k_n$ (N/mm)	$k_s$ (N/mm)
Masonry Prisms	3.41	0.2	0.43	74	–	–	6.2	0.18	1.18	–	–
Brick	6	0.15	2.1	31	–	–	–	1.22	–	–	–
Brick–Mortar joint	–	–	0.02	30	0.02	0.05	–	0.01	–	48	21
SW Materials											
Masonry Prisms	5.77	0.15	0.8	72.7	–	–	10.5	0.36	1.39	–	–
Brick	16.7	0.15	2.29	42.8	–	–	–	2	–	–	–
Brick–Mortar joint	–	–	0.35	37	0.016	0.125	–	0.25	–	82	36

simulate this wall. The results of the optimization analysis and the critical regions obtained for the three target walls are illustrated in Fig. 11, with yellow highlighting.

By examining Fig. 8, the initial value of  $C_0$  is established based on either nonlinear analysis or experimental results. The initial values of  $C_0$  for each sample, as determined from the experimental results, are presented in Fig. 12. If it is not feasible to calculate the value of  $C_0$  directly from the experimental results, an initial nonlinear analysis at the macro-scale is performed, and  $C_0$  is derived from the results of the nonlinear numerical analysis integrated into the algorithm. Additionally, Table 4 displays the values of  $C_0$  for the numerical models. The optimization algorithm identifies critical regions based on strain

energy and incorporates internal forces into each element. Consequently, the identified regions consist of areas exhibiting both stress and plastic strain.

Subsequently, as illustrated in the final steps of the flowchart presented in Fig. 3, within a two-scale numerical framework, critical regions were modeled at the meso-scale. In contrast, the remaining areas were modeled at the macro-scale. After assigning material properties, the two-scale models were analyzed using nonlinear methods. The meshing strategy for the walls is shown in Fig. 13. Additionally, the optimization parameters are outlined in Table 4.

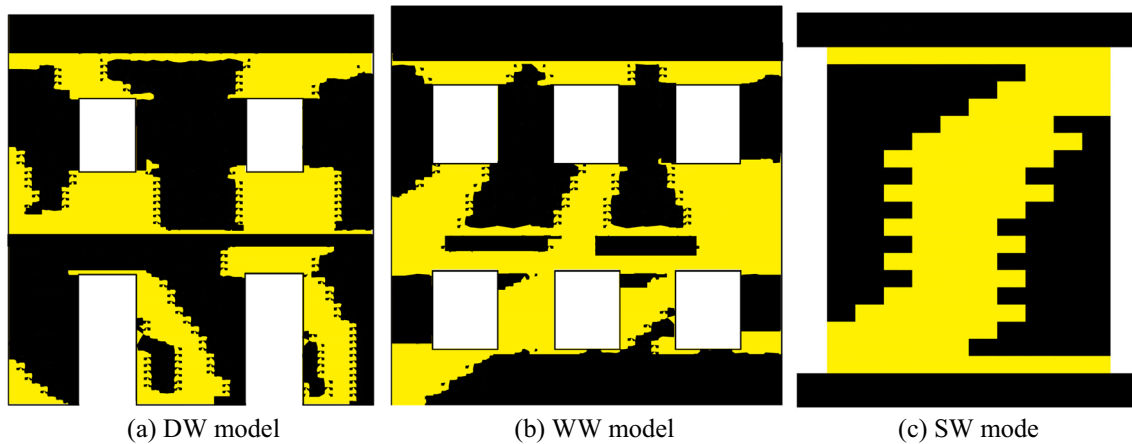


Fig. 11 Critical regions identified in the TO analysis

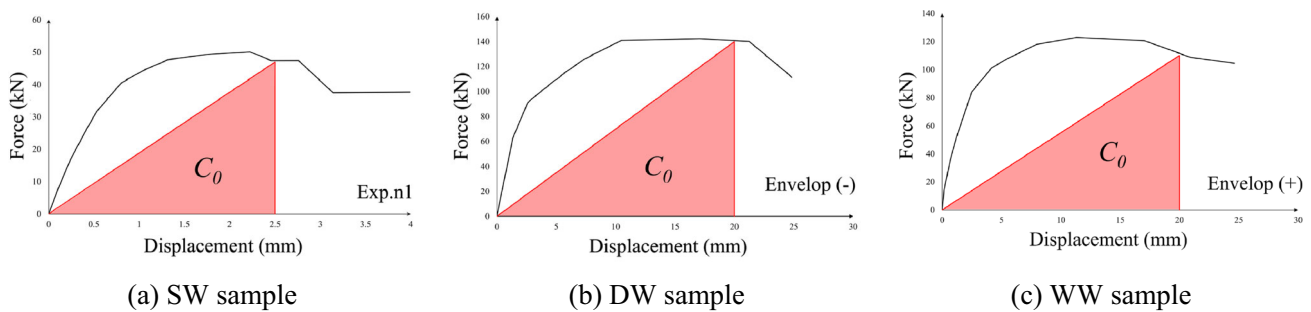


Fig. 12 Calculation of  $C_0$  based on the force–displacement diagram of experimental results

Table 4 The optimization parameters used in this problem

Numerical model	Prescribed energy $C_0$ (KJ)	Volume fraction	Linear density filter radius	Penalization parameter of SIMP
SW	0.058	40%	70 mm	3
DW	1.4			
WW	1.1			

### 4.2 Optimization Results of DW Sample

The results of the negative envelop (i.e., negative envelop refers to left to right) of the DW sample are specified in Fig. 14. It can be observed that the crack patterns in the OM model correspond to the experimental sample. This includes the initiation and propagation of cracks at the base of the wall, near the roof, between the two doors on the first floor, and under the windows on the second floor, all can be seen by the experimental results. Furthermore, by comparing the Von Mises stress contour in the OM model with the FM model, the stress distribution is accurately determined. Specifically, regions of the structure that have experienced cracking do not exhibit a stress distribution,

whereas regions that remain intact, such as the corners and around the windows, display a higher Von Mises stress intensity.

By comparing the results of MC and FM analyses, it is evident that the macro-scale models provide a reasonable approximation, accurately distributing stress. However, in the macro-scale analysis, displacements, sliding, and openings between brick elements are not observed, and a region undergoes plastic deformation. In contrast, at the meso-scale, the initiation and progression of cracking can be fully observed.

Figure 15 illustrates the lateral force–displacement diagram for the numerical models alongside the laboratory sample for both envelopes. As shown in Fig. 15, the MC model exhibits greater stiffness due to the presence of a yield surface in the DP elements, which demonstrates elastic-perfectly plastic behavior. This model does not account for the effects of sliding between elements or material softening. Consequently, the MC model displays higher stiffness values and maximum forces. In Fig. 15, the OM model shows good agreement with the experimental results; however, it exhibits higher force and initial stiffness compared to the FM model. This increase is attributed to the presence of macro-scale elements in the OM model. For the analysis of the wall in the FM, 38,794 equations

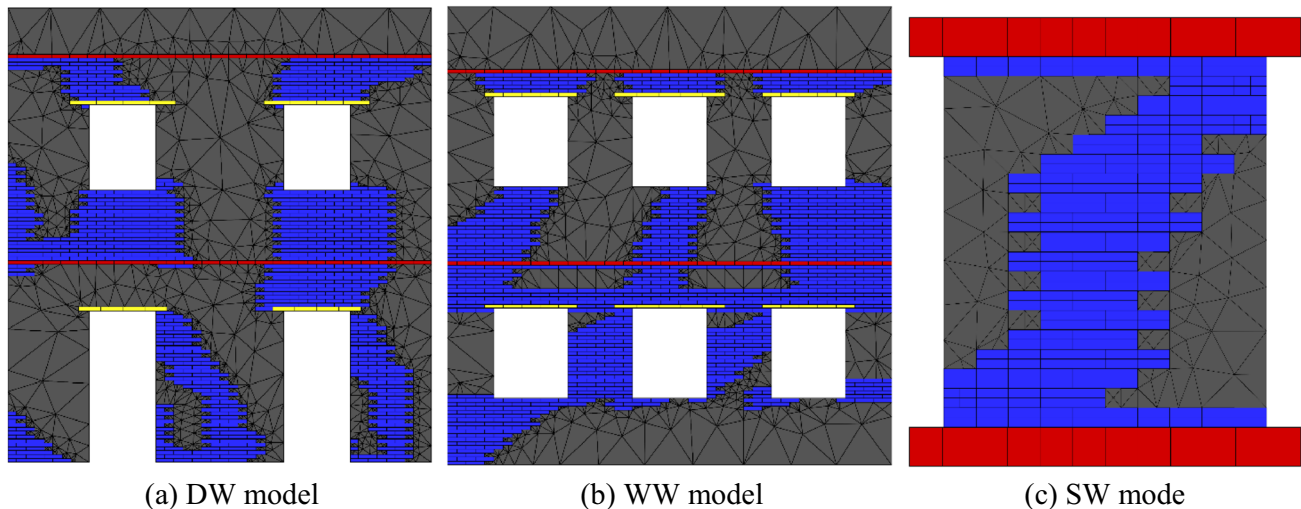


Fig. 13 The meshing strategy of OM numerical models

were solved, while 22,958 equations were solved in the OM model, and 975 calculations were performed in the MC model.

### 4.3 Optimization Results of WW Sample

The results of the positive envelope (i.e., the positive envelope refers to the right to left) of the WW sample are presented in Fig. 16. The crack pattern in the OM model closely resembles that of the experimental sample, particularly in the initiation and propagation of cracks near the roof, between the first-floor windows, and below the second-floor windows. A comparison of the Von Mises contour of the OM model with that of the FM model reveals a strong alignment in regions of high-stress intensity. Notably, the locations and stress intensities at the corners of the windows and the connection points of the roofs are consistent between the OM and FM models.

In the MC model, the stress distribution closely aligns with the results of the FM model, demonstrating appropriate accuracy. The plastic strain contour indicates that the corners of the windows are identified solely as locations of crack initiation. However, when compared to the crack pattern observed in the experimental specimen, this representation lacks sufficient accuracy. Figure 17 illustrates the force–displacement diagram for both the numerical models and the laboratory sample for each envelope.

Upon examining Fig. 17, the force–displacement diagram of the OM model demonstrates a strong correlation with both the FM model and the experimental results. In contrast, the MC model, characterized by its elastic-perfectly plastic behavior, exhibits higher values for both stiffness and maximum force. The data presented in Fig. 17 indicate that the presence of macro-scale elements in the

OM model results in greater initial stiffness and force compared to the FM model. For the analysis of wall 46,512, Equations 21,904 and 924 were solved for the FM, OM, and MC models, respectively. It is important to note that, since the WW and DW walls were subjected to cyclic testing in the laboratory, there is a slight variation in crack patterns when compared to monotonic crack patterns.

### 4.4 Optimization Results of SW Sample

The results of the SW sample analysis under controlled displacement are illustrated in Fig. 18. It is evident that in the OM model, there is a significant alignment between the crack pattern and the laboratory sample, demonstrating the accuracy of the optimization algorithm. The separation of bricks is visible in the diagonal crack. Additionally, separations can be observed at the top left and bottom right corners of the wall. When comparing the Von Mises contour between the OM and FM models, the stress distribution is accurately represented. Specifically, in the diagonal region where cracking occurs, stress is not observed; however, it is well-distributed in the vicinity of the crack region. Stress concentration is notably present in the upper right and lower left corners, as shown in Fig. 18b.

In the MC model, the stress distribution shows reasonable conformity when compared to the FM model. Additionally, the plastic strain contours closely approximate the regions of crack initiation. However, in comparison to the zones identified by the optimization algorithm, the accuracy is lower. It is important to note that the optimization analysis is conducted in a nonlinear manner. For information regarding the linear behavior of masonry, please refer to the Appendix.

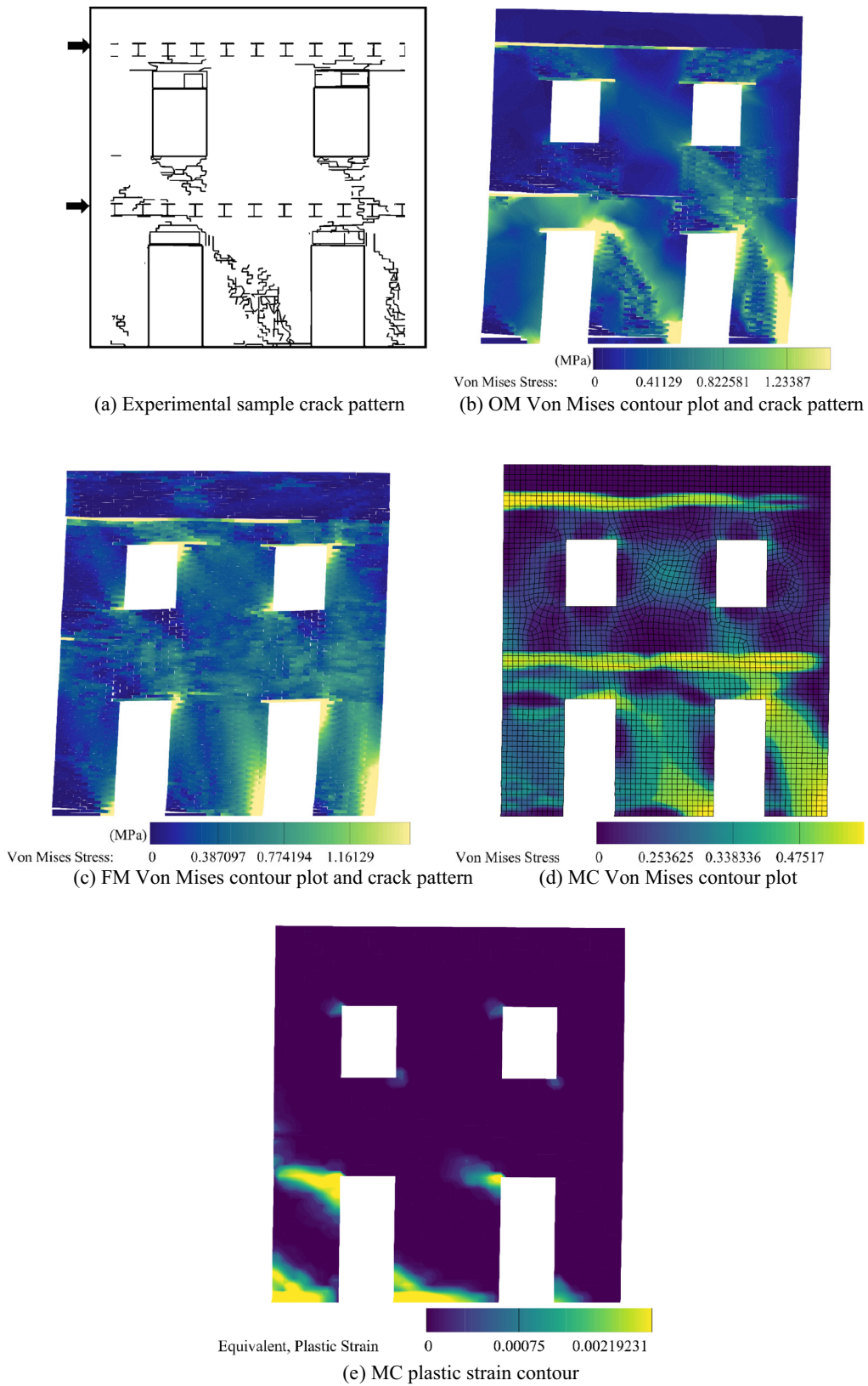
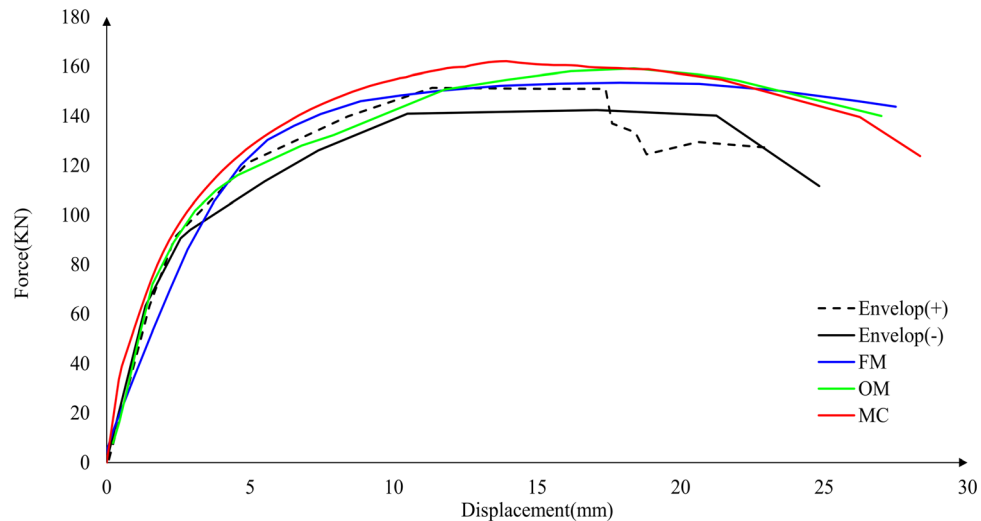


Fig. 14 Comparison of numerical model analysis results with experimental findings in the DW specimen



**Fig. 15** Comparison of lateral force–displacement of numerical models with laboratory results in both envelopes for the DW sample

In Fig. 19, the force–displacement curves of the numerical models are compared with two experimental specimens, demonstrating the effectiveness of the optimization algorithm and its accuracy in the analysis conducted. As observed in the DW and SW specimens, the MC model exhibits higher initial stiffness and maximum force compared to the other models and the experimental samples. For the analysis of this wall, 3522, 2193, and 94 equations were solved for the FM, OM, and MC models, respectively.

It is important to note that the developed method aims to reduce computational times in meso-scale analysis, and results from meso-scale and macro-scale analyses cannot be directly compared. While macro-scale analysis provides a reasonable approximation, it does not account for displacements, sliding, or opening between brick elements; instead, the entire region is treated as undergoing plastic deformation. Furthermore, many researchers have employed meso and micro-scale analyses for a detailed examination of the behavior of masonry structures [33, 71].

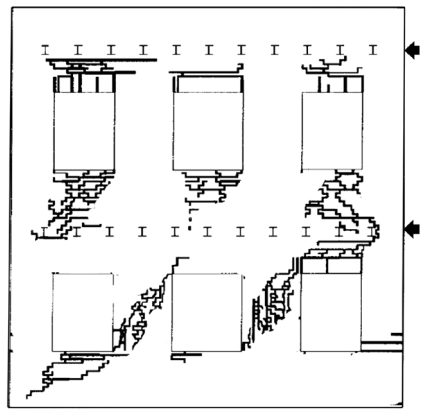
In summary, as illustrated in Figs. 15, 17, and 19, the numerical models at the macro-scale demonstrate increased stiffness. This is attributed to the incorporation of the yield surface in the DP criterion, which causes the elements to behave in an elastic-perfectly plastic manner. Consequently, these models are unable to account for the effects of sliding between elements and material softening. As a result, the reported models exhibit higher stiffness and maximum force values. Furthermore, at the macro-scale, the initiation and propagation of cracks within and between bricks remain unobservable.

#### 4.5 Computational Efficiency

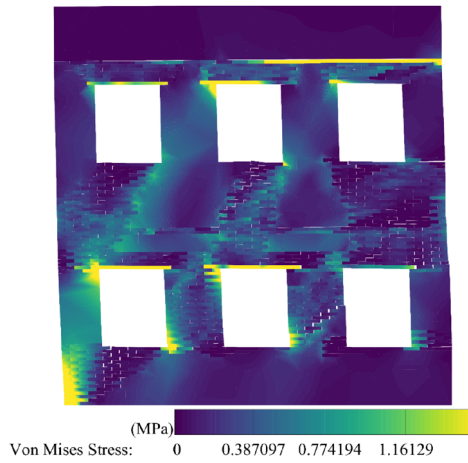
The computational time, or CPU time, plays a pivotal role in the efficiency of structural analyses, particularly when addressing complex models and extensive simulations. In the context of this research study, which involved detailed analyses of masonry buildings, CPU time emerges as a critical factor. The specifications of the computer utilized for these analyses are noteworthy. The computations were performed using an Intel i5-13600 K processor operating at 3.5 GHz, equipped with 32 GB DDR5 RAM and an SSD hard drive featuring a data reading speed of 560 MB/s and a data writing speed of 530 MB/s. These robust hardware specifications facilitated the efficient execution of the structural analyses.

Table 5 presents the computational costs associated with the analyzed numerical models, offering a comparative analysis of the number of elements, nodes, equations, and CPU time across three distinct models (DW, WW, SW) using various methods (FM, OM, TO, MC). Additionally, this table incorporates several quantitative indices that have been calculated to evaluate model performance, including the Normalized CPU Time (NCT), Maximum Load Accuracy Index (MLAI), and Combined Accuracy-Efficiency Index (CAEI). Collectively, these indices provide a comprehensive assessment of both computational efficiency and accuracy.

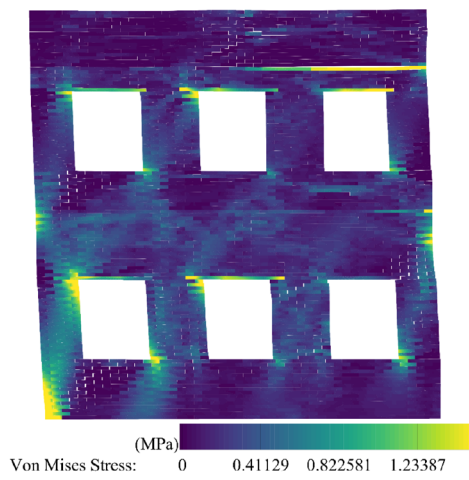
As shown in Table 5, the OM models exhibit a significant reduction in the number of nodes and elements compared to the FM models, with reductions of 40.8% for the DW model, 52.9% for the WW model, and 37.7% for the



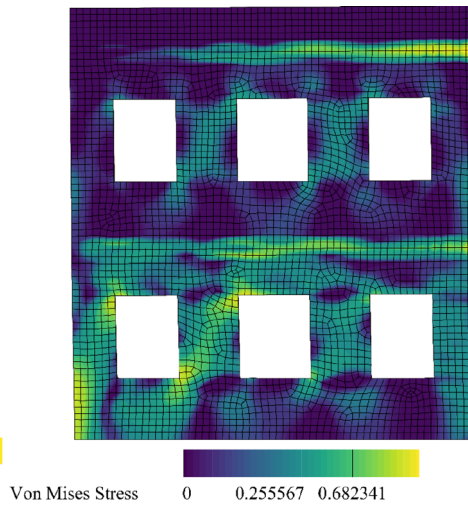
(a) Experimental sample crack pattern



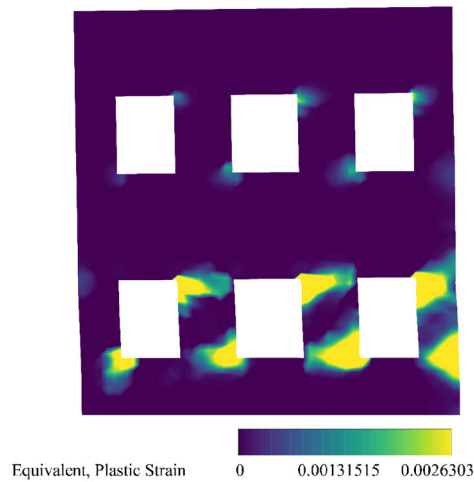
(b) OM Von Mises contour plot and crack pattern



(c) FM Von Mises contour plot and crack pattern



(d) MC Von Mises contour plot



(e) MC plastic strain contour

Fig. 16 Comparison of numerical model analysis results with experimental findings in the WW specimen

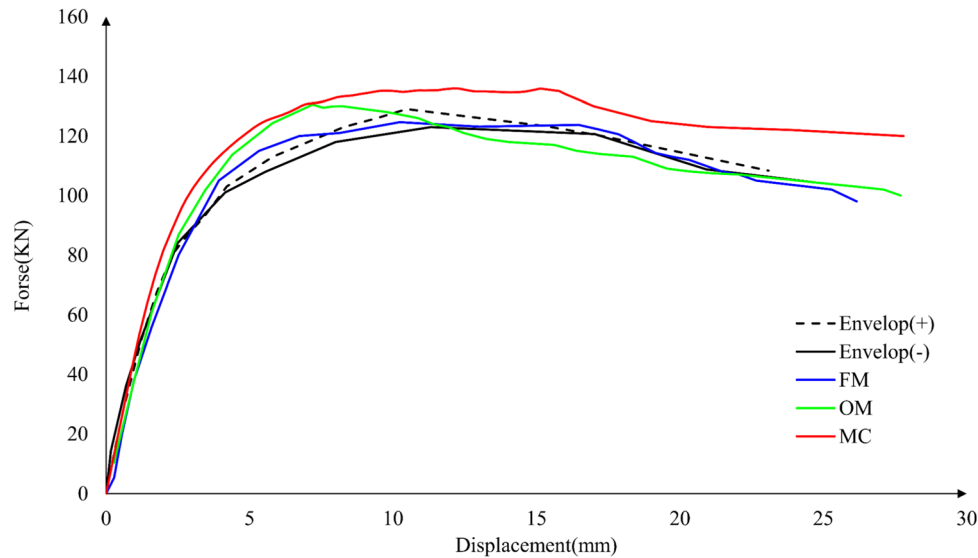


**Fig. 17** Comparison of lateral force–displacement of numerical models with laboratory results in both envelopes for the WW sample

SW model. However, due to the iterative nature of the TO process at the macro scale, evaluating computational costs based solely on the number of nodes is less appropriate. A more accurate assessment should involve analyzing the number of equations solved, CPU time, and the various quantitative indices.

For the DW sample, the MC model was computed in 176 s, as specified by the hardware specifications. In contrast, the computations for the FM model took 7001.9 s, which is approximately 50 times longer, demonstrating a significant difference in CPU time between these two scales. The numerical modeling of samples using the methodology developed in this research resulted in fewer equations being computed. Specifically, the TO process computations for the DW sample required 576 s, while the OM model took 4143.67 s.

In the WW sample, the MC model was analyzed in 168 s, while the FM model computations required 8395 s, also about 50 times longer. The TO process for this sample was completed in 579 s, whereas the OM model took 3953 s.

Similarly, in the SW sample, the MC model was analyzed in just 17.2 s, while the FM model computations required 635.68 s—approximately 37 times longer. The TO process for this sample took 55 s, and the OM model was computed in 395.81 s.

The NCT was assessed for each sample to quantify the computational efficiency of the OM models relative to the FM model, as shown in Eq. (37). To effectively compare the computational efficiency of the method, it is crucial to consider the total CPU time for both phases (TO + OM)

and compare it with the FM model. A lower NCT signifies higher computational efficiency.

$$NCT = \frac{CPU\ Time_{OM+TO}}{CPU\ Time_{FM}} \quad (37)$$

For the DW sample, the NCT was approximately 0.67. In the WW sample, the NCT value was around 0.54, and for the SW sample, the NCT was approximately 0.71. These values underscore the significant computational efficiency achieved through the proposed method in comparison to the FM model.

The CPU time reduction can be determined using Eq. (38). Applying this, the CPU time reduction for the DW sample is approximately 33%, for the WW sample about 46%, and for the SW sample around 29%. These values illustrate the substantial computational cost savings realized by the OM models compared to the FM models, showcasing the efficiency of the process while maintaining high accuracy.

$$CPU\ Time\ Reduction\ (\%) = (1 - NCT) \times 100 \quad (38)$$

To further enhance the understanding of the accuracy and efficiency of the models, the MLAI was defined to measure the closeness of the maximum load from OM to the experimental results, calculated as shown in Eq. (39). Here, a value of MLAI close to 1 indicates high accuracy in replicating the experimental maximum load. For the DW sample, the MLAI was approximately 0.86, indicating an accuracy of 86%. In the WW sample, the MLAI reached 0.93, demonstrating 93% accuracy, while the SW sample exhibited the highest accuracy, with an MLAI of 0.98.

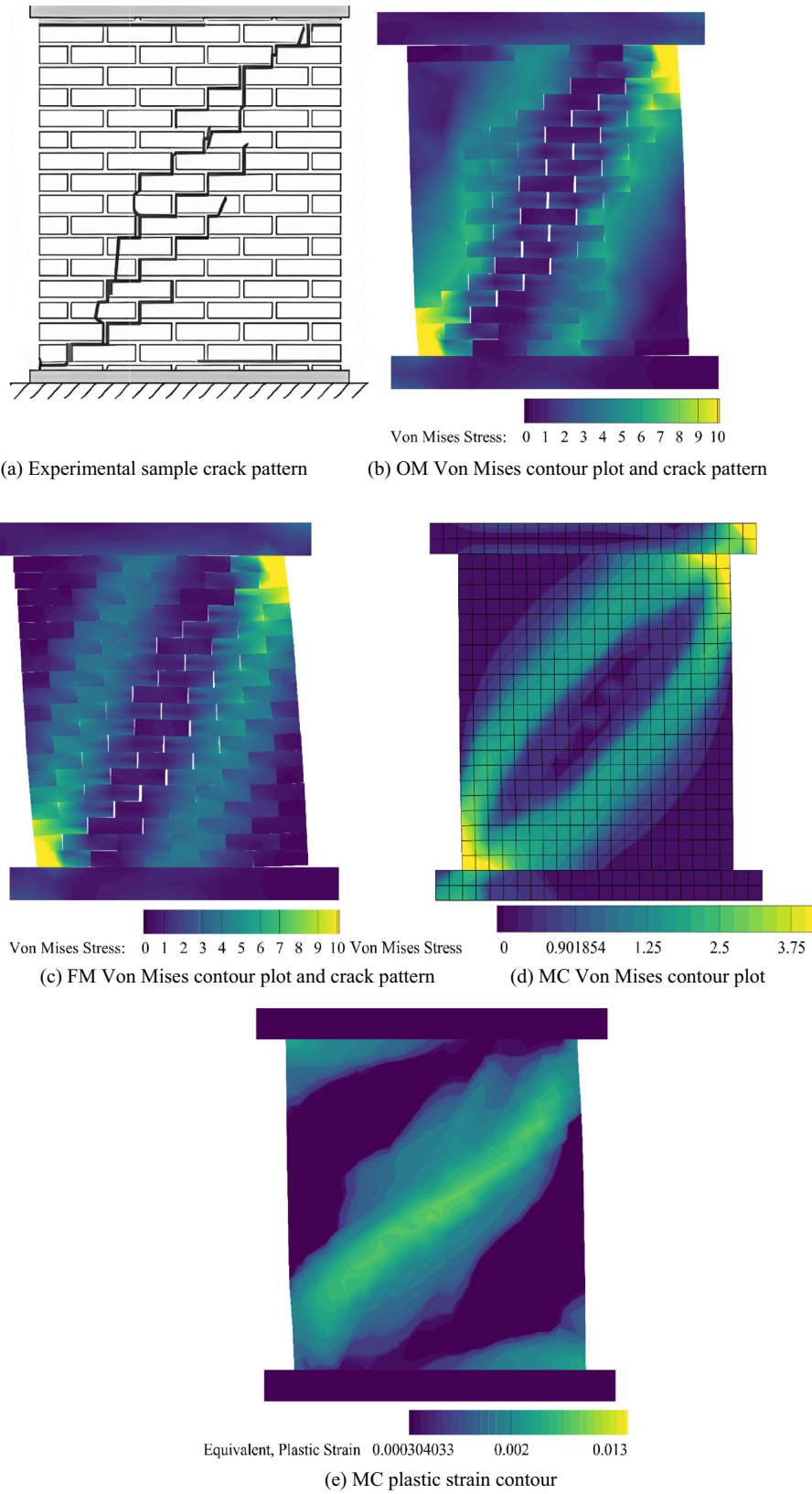


Fig. 18 Comparison of numerical model analysis results with experimental findings in the SW specimen

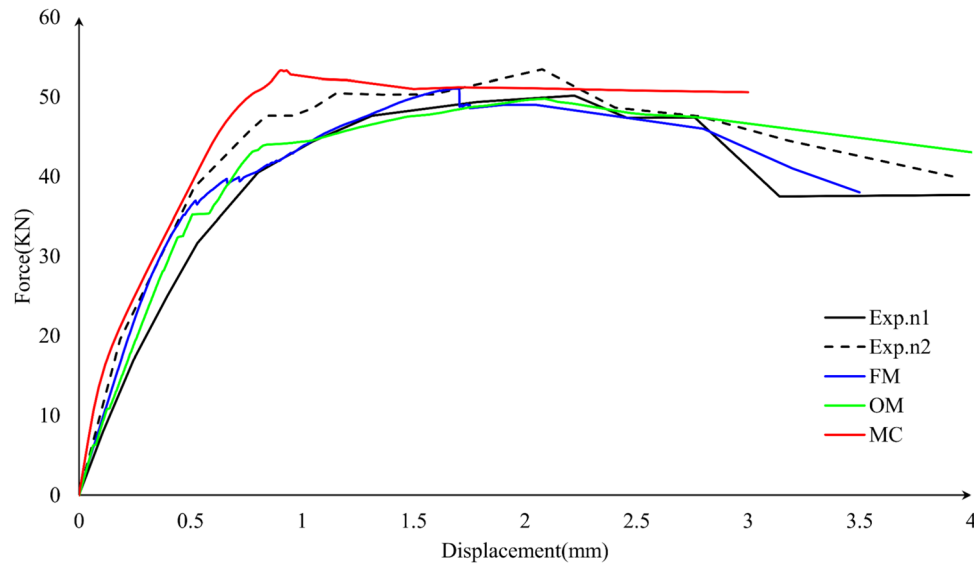


Fig. 19 Comparison of lateral force–displacement of numerical models with laboratory results for the SW sample

Table 5 Computational costs and quantitative indices of the analyzed numerical models

Model	DW model				WW model				SW model			
	FM	OM	TO	MC	FM	OM	TO	MC	FM	OM	TO	MC
Number of elements	43,643	5101	216	216	52,326	4867	205	205	3962	2598	21	21
Number of nodes	19,397	11,479	487	487	23,256	10,952	462	462	1761	1096	47	47
Number of Eq.s	38,794	22,958	3191	975	46,512	21,904	3041	924	3522	2193	304	94
CPU time (sec)	7001.9	4143.67	576	176	8395	3953	549	168	635.68	396	55	17
NCT	0.67				0.54				0.71			
CPU time Reduction	33%				46%				29%			
MLAI	0.86				0.93				0.98			
CAEI	0.28				0.43				0.28			

$$MLAI = 1 - \frac{|Max Load_{OM} - Max Load_{Exp}|}{Max Load_{Exp}} \quad (39)$$

Additionally, the CAEI was calculated for each sample to balance accuracy and computational efficiency, defined as shown in Eq. (40). A CAEI value close to 1 indicates both high accuracy and computational efficiency. For the DW sample, the CAEI was approximately 0.28; for the SW sample, it was also 0.28; and for the WW sample, it reached 0.43. This higher CAEI value for the WW sample demonstrates a better overall balance of accuracy and efficiency. These results underscore the effectiveness of the OM models in replicating experimental maximum loads while maintaining lower computational costs compared to the FM models.

$$CAEI = MLAI \times (1 - NCT) \quad (40)$$

## 5 Conclusions

This research study presents an algorithm developed to reduce the computational time associated with the analysis of meso-scale masonry buildings. The algorithm, which is based on nonlinear topology optimization and utilizes the DP yield surface, aims to balance computational efficiency and accuracy in the numerical modeling of masonry structures at the meso-scale. The key innovation lies in the optimization process, where critical regions responsible for effective force transmission are identified during the

nonlinear macro-scale analysis. Subsequently, a two-scale model is generated, with these critical regions modeled at the meso-scale while the remaining sections are retained at the macro-scale. To evaluate the efficiency of the developed algorithm, three samples of masonry walls were analyzed, and the results were compared in terms of computational time and accuracy across the meso-scale, macro-scale, and optimized meso-scale. The following results were obtained.

- The developed method significantly reduced computational time (i.e., CPU time) without compromising the accuracy of the analysis results. Furthermore, the optimized meso-scale models demonstrated a high level of accuracy in representing crack patterns, closely aligning with the experimental samples. In summary, the developed algorithm not only enhances cost-efficiency but also ensures precision in capturing the complex behavior of masonry structures under various loading conditions.
- Macro-scale models exhibited lower accuracy compared to meso-scale models and demonstrated greater initial stiffness and maximum force due to their elastic-perfectly plastic behavior. This highlights the significance of modeling these structures at the meso-scale.
- In the DW sample, the macro-scale model required 176 s for computation, while the full meso-scale model computations took 7001.9 s. The optimization process for this sample lasted 576 s, and the optimized meso-scale model computations took 4143.67 s, indicating a 32.5% reduction in computational time compared to the full meso-scale model. CAEI was approximately **0.28**, highlighting a balance between accuracy and computational efficiency.
- In the WW sample, the macro-scale model analysis lasted 168 s, while the full meso-scale model computations took 8,395 s. The optimization process for this sample required 579 s, compared to 3,953 s for the optimized meso-scale model, demonstrating a 46% reduction in computational time relative to the full meso-scale model. the CAEI was 0.43, indicating a better overall balance of accuracy and efficiency.
- In the SW sample, the macro-scale model analysis lasted 17.2 s, while the full meso-scale model computations took 635.68 s. The optimization process for this sample required 55 s, and the optimized meso-scale model computations lasted 395.81 s, indicating a 30% reduction in computational cost compared to the full meso-scale model. CAEI was approximately **0.28**, highlighting a balance between accuracy and computational efficiency.

## Appendix

### Linear Topology Optimization

The developed algorithm takes into account the nonlinear behavior of materials. In the linear TO scenario, the objective is to minimize strain energy in order to reduce material volume. Since minimizing energy is equivalent to maximizing structural stiffness in regions experiencing the highest stress, the general relationship is defined as follows [72, 73]:

$$\begin{aligned} U_c &= a \text{ minimum } \eta_i \\ \text{subject to } 0 &< \eta_i \leq 1 \quad (i = 1, 2, 3, \dots, N) \\ V &\leq V_0 - V^* \end{aligned} \quad (41)$$

In Eq. (41),  $\eta_i$  represents the optimization coefficient for each element,  $V$  is the volume of the finite element model,  $V_0$  is the initial volume, and  $V^*$  is the material volume that needs to be removed. TO may be based on one or several loading combinations. Accordingly, the stiffness value  $K$  in each loading combination is calculated by applying weighting coefficients as per the following relationship:

$$F(U_c^1, U_c^2, \dots, U_c^k) = \sum_{i=1}^k W_i U_c^i, \quad W_i \geq 0 \quad (42)$$

In Eq. (42),  $W_i$  is the weighting coefficient for each loading combination based on  $U_c$ . Subsequently, the total volume of the elements is calculated according to the following relationship:

$$\begin{aligned} V &= \sum_i \eta_i V_i \\ [E] &= [E(\eta_i)] \{ \sigma_i \} = [E] \{ \varepsilon_i \} \end{aligned} \quad (43)$$

In Eq. (43),  $V_i$  represents the volume of the  $i$ -th element. Considering that the value of the elastic modulus tensor is dependent on the tensor of each element, it follows that the elastic modulus tensor is influenced by the stress and strain tensors. Consequently, it can be concluded that the elements most critical to a problem will experience the highest levels of stress and strain, thereby increasing the likelihood of crack propagation in these regions.

If the behavior of the masonry is assumed to be linear, the regions resulting from the TO analysis for the SW sample are illustrated in Fig. 20. Based on the stress contours and the optimized analysis regions, it is evident that when the behavior of the brittle material is considered linearly, the areas where the material fails in tension are not accounted for in the algorithm.

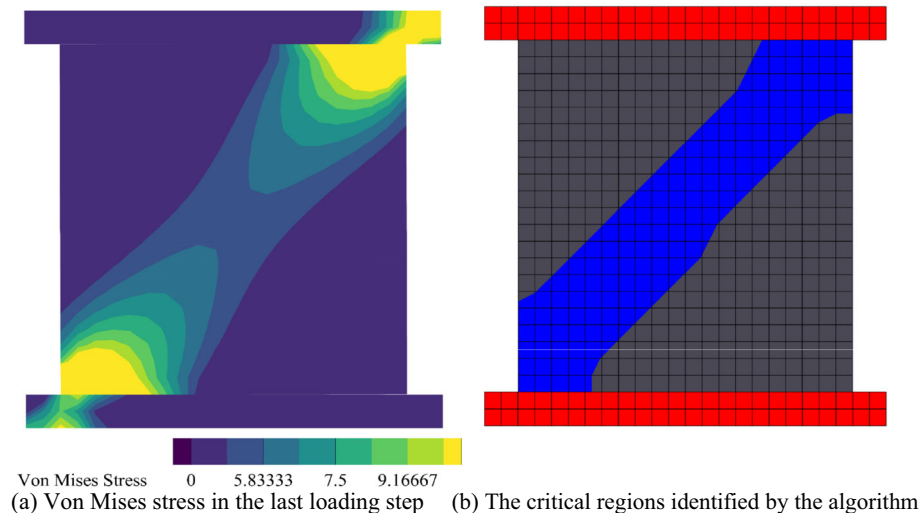


**Fig. 20** The optimization results obtained by the TO of the SW specimen in the linear state

## Declarations

**Conflict of interest** The authors declare that there is no conflict of interest regarding the publication of this paper.

**Open Access** This article is licensed under a Creative Commons Attribution 4.0 International License, which permits use, sharing, adaptation, distribution and reproduction in any medium or format, as long as you give appropriate credit to the original author(s) and the source, provide a link to the Creative Commons licence, and indicate if changes were made. The images or other third party material in this article are included in the article's Creative Commons licence, unless indicated otherwise in a credit line to the material. If material is not included in the article's Creative Commons licence and your intended use is not permitted by statutory regulation or exceeds the permitted use, you will need to obtain permission directly from the copyright holder. To view a copy of this licence, visit <http://creativecommons.org/licenses/by/4.0/>.

## References

- Bendsoe MP, Sigmund O (2003) Topology optimization—theory, methods, and applications. Springer
- Bendsoe MP (1989) Optimal shape design as a material distribution problem. *Structural Optimization* 1(4):193–202. <https://doi.org/10.1007/BF01650949>
- Wu J, Sigmund O, Groen JP (2021) Topology optimization of multi-scale structures: a review. *Struct Multidiscip Optim* 63(3):1455–1480. <https://doi.org/10.1007/s00158-021-02881-8>
- Yago D, Cante J, Lloberas-Valls O, Oliver J (2022) Topology optimization methods for 3D structural problems: a comparative study. *Arch Comput Methods Eng* 29(3):1525–1567. <https://doi.org/10.1007/s11831-021-09626-2>
- Wei P, Yang Y, Chen S, Wang MY (2021) A study on basis functions of the parameterized level set method for topology optimization of continua. *J Mech Design*. <https://doi.org/10.1115/14047900>
- Xie YM, Steven GP (1996) Evolutionary structural optimization for dynamic problems. *Comput Struct* 58(6):1067–1073. [https://doi.org/10.1016/0045-7949\(95\)00235-9](https://doi.org/10.1016/0045-7949(95)00235-9)
- Bendsoe MP, Kikuchi N (1988) Generating optimal topologies in structural design using a homogenization method. *Comput Methods Appl Mech Eng* 71:197–224
- Zhou Q, Shen W, Wang J, Zhou YY, Xie YM (2018) Ameba: a new topology optimization tool for architectural design. In: *Proceedings of IASS Annual Symposia*, Vol. 2018. International Association for Shell and Spatial Structures (IASS), pp. 1–8
- Yang XY, Xie YM, Steven GP, Querin OM (1999) Bidirectional evolutionary method for stiffness optimization. *AIAA J* 37:1483–1488. <https://doi.org/10.2514/3.14346>
- Zhao ZL, Zhou S, Feng XQ, Xie YM (2020) Morphological optimization of scorpion telson. *J Mech Phys Solids*. <https://doi.org/10.1016/j.jmps.2019.103773>
- Razvan C (2014) Overview of structural topology optimization methods for plane and solid structures. *Annals of the oradea universitY. Fascicle Manag Technol Eng*. <https://doi.org/10.15660/auofmte.2014-3.3043>
- Harzheim L, Graf G (2005) A review of optimization of cast parts using topology optimization: I—topology optimization without manufacturing constraints. *Struct Multidiscip Optim* 30(6):491–497. <https://doi.org/10.1007/s00158-005-0553-x>
- Shimoda M, Umemura M, Al Ali M, Tsukihara R (2023) Shape and topology optimization method for fiber placement design of CFRP plate and shell structures. *Compos Struct* 309:116729. <https://doi.org/10.1016/j.compstruct.2023.116729>
- Tarhan İH, Uysal H (2023) Topology optimization of the FRP for strengthening of masonry barrel vaults. *Eng Fail Anal*. <https://doi.org/10.1016/j.engfailanal.2023.107390>
- Permanoon A, Akhaveissy AH (2022) Failure of existing structures with semi-brittle mechanical properties on meso scale and reduction of computational cost using non-linear topology optimization. *Constr Building Mater*. <https://doi.org/10.1016/j.conbuildmat.2021.126071>
- Latifi R, Hadzima-Nyarko M, Radu D, Rouhi R (2023) A brief overview on crack patterns, repair and strengthening of historical masonry structures. *Materials*. <https://doi.org/10.3390/ma16051882>

17. Adhikari RK, Parammal Vatteri A, D'Ayala D (2023) Seismic performance assessment of low-rise unreinforced and confined brick masonry school buildings using the applied element method. *Buildings*. <https://doi.org/10.3390/buildings13010159>
18. Gregori A, Mercuri M, Angiolilli M, Pathirage M (2022) Simulating defects in brick masonry panels subjected to compressive loads. *Eng Struct*. <https://doi.org/10.1016/j.engstruct.2022.114333>
19. Dltri AM, Sarhosis V, Milani G, Rots J, Cattari S, Lagomarsino S, de Miranda S (2020) Modeling strategies for the computational analysis of unreinforced masonry structures: review and classification. *Archives of computational methods in engineering*, vol 27. Springer, Netherlands
20. Al-fakih A, Al-osta MA (2022) Finite element analysis of rubberized concrete interlocking masonry under vertical loading. *Materials* 15(8):2858. <https://doi.org/10.3390/ma15082858>
21. Weber M, Thoma K, Hofmann J (2021) Finite element analysis of masonry under a plane stress state. *Eng Struct*. <https://doi.org/10.1016/j.engstruct.2020.111214>
22. Zeng B, Li Y, Cruz Noguez C (2021) Modeling and parameter importance investigation for simulating in-plane and out-of-plane behaviors of un-reinforced masonry walls. *Eng Struct*. <https://doi.org/10.1016/j.engstruct.2021.113233>
23. Duarte APC, Silva BA, Silvestre N, De Brito J, Júlio E (2015) Mechanical characterization of rubberized concrete using an image-processing/XFEM coupled procedure. *Compos B Eng* 78:214–226. <https://doi.org/10.1016/j.compositesb.2015.03.082>
24. Lubliner J, Oliver J, Oller S, Oñate E (1989) A plastic-damage model for concrete. *Int J Solids Struct* 25(3):299–326. [https://doi.org/10.1016/0020-7683\(89\)90050-4](https://doi.org/10.1016/0020-7683(89)90050-4)
25. Zhao X, Dong Q, Chen X, Ni F (2021) Meso-cracking characteristics of rubberized cement-stabilized aggregate by discrete element method. *J Cleaner Prod*. <https://doi.org/10.1016/j.jclepro.2021.128374>
26. Asad M, Zahra T, Thamboo J, Song M (2022) Finite element modelling of reinforced masonry walls under axial compression. *Eng Struct*. <https://doi.org/10.1016/j.engstruct.2021.113594>
27. Koocheki K, Pietruszczak S (2023) Numerical analysis of large masonry structures: bridging meso and macro scales via artificial neural networks. *Comput Struct*. <https://doi.org/10.1016/j.compstruc.2023.107042>
28. Pulatsu B, Erdogmus E, Lourenço PB, Lemos JV, Tuncay K (2020) Simulation of the in-plane structural behavior of unreinforced masonry walls and buildings using DEM. *Structures*, vol 27. Elsevier, pp 2274–2287
29. Akhveissy AH (2013) Limit state strength of unreinforced masonry structures. *Earthq Spectra* 29(1):1–31. <https://doi.org/10.1193/1.4000097>
30. Dolatshahi KM, Aref AJ (2011) Two-dimensional computational framework of meso-scale rigid and line interface elements for masonry structures. *Eng Struct* 33(12):3657–3667. <https://doi.org/10.1016/j.engstruct.2011.07.030>
31. Chisari C, Macorini L, Amadio C, Izzuddin BA (2018) Identification of mesoscale model parameters for brick-masonry. *Int J Solids Struct* 146:224–240. <https://doi.org/10.1016/j.ijsolstr.2018.04.003>
32. Tubaldi E, Minga E, Macorini L, Izzuddin BA (2020) Mesoscale analysis of multi-span masonry arch bridges. *Eng Struct*. <https://doi.org/10.1016/j.engstruct.2020.111137>
33. Akhveissy AH, Permannoon A, Raeisi R (2021) Numerical modeling of masonry wall under underground waves. *Scientia Iranica*. <https://doi.org/10.24200/sci.2021.53605.3327>
34. Lourenço PB, Silva LC (2020) Computational applications in masonry structures: from the meso-scale to the super-large/super-complex. *Int J Multiscale Comput Eng* 18(1):1–30. <https://doi.org/10.1615/IntJMultCompEng.2020030889>
35. Maccarini H, Vasconcelos G, Rodrigues H, Ortega J, Lourenço PB (2018) Out-of-plane behavior of stone masonry walls: experimental and numerical analysis. *Constr Build Mater* 179:430–452. <https://doi.org/10.1016/j.conbuildmat.2018.05.216>
36. Mercuri M, Pathirage M, Gregori A, Cusatis G (2020) Computational modeling of the out-of-plane behavior of unreinforced irregular masonry. *Eng Struct* 223:111181. <https://doi.org/10.1016/j.engstruct.2020.111181>
37. Addessi D, Di Re P, Gatta C, Sacco E (2022) Shell-3D multiscale modeling of masonry vaults based on the tfa procedure. *Int J Multiscale Comput Eng* 20(6):13–42. <https://doi.org/10.1615/IntJMultCompEng.2022041774>
38. Addessi D, Di Re P, Gatta C, Sacco E (2021) Multiscale analysis of out-of-plane masonry elements using different structural models at macro and microscale. *Comput Struct*. <https://doi.org/10.1016/j.compstruc.2020.106477>
39. Addessi D, Di Re P, Sacco E (2020) Micromechanical and multiscale computational modeling for stability analysis of masonry elements. *Eng Struct* 211(2019):110428. <https://doi.org/10.1016/j.engstruct.2020.110428>
40. Petracca M, Pelà L, Rossi R, Oller S, Camata G, Spacone E (2017) Multiscale computational first order homogenization of thick shells for the analysis of out-of-plane loaded masonry walls. *Comput Methods Appl Mech Eng* 315:273–301. <https://doi.org/10.1016/j.cma.2016.10.046>
41. Mercatoris BCN, Massart TJ (2011) A coupled two-scale computational scheme for the failure of periodic quasi-brittle thin planar shells and its application to masonry. *Int J Numer Meth Eng* 85(9):1177–1206. <https://doi.org/10.1002/nme.3018>
42. Sivapuram R, Dunning PD, Kim HA (2016) Simultaneous material and structural optimization by multiscale topology optimization. *Struct Multidiscip Optim* 54(5):1267–1281. <https://doi.org/10.1007/s00158-016-1519-x>
43. Akhveissy AH, Permannoon A (2022) An investigation of meso-scale crack propagation process in concrete beams using topology optimization. *Amirkabir J Civil Eng* 53(12):5281–5306
44. Permannoon A, Akhveissy AH (2019) Effects of meso-scale modeling on concrete fracture parameters calculation. *Periodica Polytechnica Civil Eng* 63(3):782–794. <https://doi.org/10.3311/PPci.13874>
45. Wang MY, Wang X, Guo D (2003) A level set method for structural topology optimization. *Comput Methods Appl Mech Eng* 192(1–2):227–246. [https://doi.org/10.1016/S0045-7825\(02\)00559-5](https://doi.org/10.1016/S0045-7825(02)00559-5)
46. Banh TT, Lee D (2018) Multi-material topology optimization design for continuum structures with crack patterns. *Compos Struct* 186:193–209. <https://doi.org/10.1016/j.compstruct.2017.11.088>
47. Drucker DC, Prager W (1952) Soil mechanics and plastic analysis or limit design. *Q Appl Math* 10(2):157–165. <https://doi.org/10.1090/qam/48291>
48. Chen WF, Han DJ (1988) *Plasticity for structural engineers*. Plasticity for structural engineers. J. Ross publishing. <https://doi.org/10.1007/978-1-4612-3864-5>
49. Luo Y, Kang Z (2012) Topology optimization of continuum structures with Drucker-Prager yield stress constraints. *Comput Struct* 90–91(1):65–75. <https://doi.org/10.1016/j.compstruc.2011.10.008>
50. Tomazevic M (1999) Earthquakes and seismic performance of masonry buildings, pp. 5–33. [https://doi.org/10.1142/9781848160835\\_0002](https://doi.org/10.1142/9781848160835_0002)
51. (US), BSSC, Council AT (1997) NEHRP guidelines for the seismic rehabilitation of buildings, Vol. 1. Federal Emergency Management Agency

52. Lelovic S, Vasovic D (2020) Determination of mohr-coulomb parameters for modelling of concrete. *Crystals* 10(9):1–16. <https://doi.org/10.3390/cryst10090808>
53. NASTRI E, TODISCO P (2022) Macromechanical failure criteria: elasticity, plasticity and numerical applications for the non-linear masonry modelling. *Buildings*. <https://doi.org/10.3390/buildings12081245>
54. Zhao T, Lages EN, Ramos AS, Paulino GH (2020) Topology optimization considering the Drucker-Prager criterion with a surrogate nonlinear elastic constitutive model. *Struct Multidiscip Optim*. <https://doi.org/10.1007/s00158-020-02671-8>
55. Hencky H (1924) Zur Theorie plastischer Deformationen und der hierdurch im Material hervorgerufenen Nachspannungen. *ZAMM-J Appl Math Mech/Zeitschrift für Angewandte Mathematik und Mechanik* 4(4):323–334
56. Sonato M, Piccolroaz A, Miszuris W, Mishuris G (2015) General transmission conditions for thin elasto-plastic pressure-dependent interphase between dissimilar materials. *Int J Solids Struct* 64:9–21
57. Zhao T, Ramos AS, Paulino GH (2019) Material nonlinear topology optimization considering the von Mises criterion through an asymptotic approach: max strain energy and max load factor formulations. *Int J Numer Meth Eng* 118(13):804–828. <https://doi.org/10.1002/nme.6038>
58. Niu F, Xu S, Cheng G (2011) A general formulation of structural topology optimization for maximizing structural stiffness. *Struct Multidiscip Optim* 43(4):561–572. <https://doi.org/10.1007/s00158-010-0585-8>
59. Klarbring A, Strömberg N (2012) A note on the min-max formulation of stiffness optimization including non-zero prescribed displacements. *Struct Multidiscip Optim* 45(1):147–149. <https://doi.org/10.1007/s00158-011-0674-3>
60. Li L, Khandelwal K (2017) Design of fracture resistant energy absorbing structures using elastoplastic topology optimization. *Struct Multidiscip Optim* 56(6):1447–1475. <https://doi.org/10.1007/s00158-017-1735-z>
61. Menétrey P (1994) Numerical analysis of punching failure in reinforced concrete structures. Thesis, 156. Retrieved from <http://infoscience.epfl.ch/record/31757>. Accessed 16 Mar 2005
62. Menétrey P (2002) Synthesis of punching failure in reinforced concrete. *Cement Concr Compos* 24(6):497–507. [https://doi.org/10.1016/S0958-9465\(01\)00066-X](https://doi.org/10.1016/S0958-9465(01)00066-X)
63. Alfano G, Crisfield MA (2001) Finite element interface models for the delamination analysis of laminated composites: mechanical and computational issues. *Int J Numer Meth Eng* 50(7):1701–1736. <https://doi.org/10.1002/nme.93>
64. Park K, Paulino GH (2011) Cohesive zone models: a critical review of traction-separation relationships across fracture surfaces. *Appl Mech Rev*. <https://doi.org/10.1115/1.4023110>
65. Nguyen VP, Lian H, Rabczuk T, Bordas S (2017) Modelling hydraulic fractures in porous media using flow cohesive interface elements. *Eng Geol* 225:68–82. <https://doi.org/10.1016/j.enggeo.2017.04.010>
66. Computed tomography images based phase- field modeling of mesoscopic failure in concrete. (n.d.)
67. Magenes G, Calvi GM, Kingsley GR (1995) Seismic testing of a full-scale, two-storey masonry building: test procedure and measured experimental response. Experimental and numerical investigation on a brick masonry building-prototype—Numerical prediction of the experiment, Report 3.0—G.N.D.T. <https://doi.org/10.13140/RG.2.1.4590.2962>
68. Roberti GM, Binda L, Cardani G (2020) Numerical modeling of shear bond tests on small brick-masonry assemblages. In: Press CRC (ed) *Computer methods in structural masonry—4*, vol 4. pp 156–164
69. Scrivener JC (1982) Shear tests on reinforced brick masonry walls. Technical Note—British Ceramic Res Assoc 342:55
70. Petracca M, Pelà L, Rossi R, Zaghi S, Camata G, Spacone E (2017) Micro-scale continuous and discrete numerical models for nonlinear analysis of masonry shear walls. *Constr Build Mater* 149:296–314. <https://doi.org/10.1016/j.conbuildmat.2017.05.130>
71. Minga E (2017) 3D Meso- and macro-scale models for nonlinear analysis of masonry systems, (September), 305
72. Li Q, Steven GP, Xie YM (1999) On equivalence between stress criterion and stiffness criterion in evolutionary structural optimization. *Structural Optimization* 18(1):67–73. <https://doi.org/10.1007/BF01210693>
73. McKeown JJ (1997) A note on the equivalence between maximum stiffness and maximum strength trusses. *Eng Optim* 29(1–4):443–456. <https://doi.org/10.1080/03052159708941007>